

2022

Investigation of giant vacuoles in the inner wall endothelium of Schlemm's canal at physiologic pressure and comparison of the types and size of giant vacuoles in human eyes perfused at 7- and 15-mm Hg using serial block-face scanning electron microscopy

---

<https://hdl.handle.net/2144/45667>

*"Downloaded from OpenBU. Boston University's institutional repository."*

BOSTON UNIVERSITY  
SCHOOL OF MEDICINE

Thesis

**INVESTIGATION OF GIANT VACUOLES IN THE INNER WALL  
ENDOTHELIUM OF SCHLEMM'S CANAL AT PHYSIOLOGIC PRESSURE  
AND COMPARISON OF THE TYPES AND SIZE OF GIANT VACUOLES IN  
HUMAN EYES PERFUSED AT 7- AND 15-MM HG USING SERIAL BLOCK-  
FACE SCANNING ELECTRON MICROSCOPY**

by

**BENJAMIN L. SOARES**

B.A., Boston University, 2020

Submitted in partial fulfillment of the  
requirements for the degree of  
Master of Science

2022

© 2022 by  
BENJAMIN L. SOARES  
All rights reserved

Approved by

First Reader

---

Haiyan Gong, M.D., Ph.D.  
Professor of Ophthalmology, Anatomy, and Neurobiology

Second Reader

---

Andrew W. Taylor, Ph.D.  
Associate Dean of Research  
Professor of Ophthalmology

*“As the circle of light grows larger, so also does the perimeter of darkness”*

*– Albert Einstein*

## **DEDICATION**

I would like to dedicate this work to my family; Mom, Dad, Sam and Jake for supporting and inspiring me.

## ACKNOWLEDGMENTS

I'd like to acknowledge Dr. Haiyan Gong and members of the Gong laboratory for teaching me the ropes, assisting in my research and being great friends. I'm grateful to David Swain for trailblazing giant vacuole research using SBF-SEM. I believe that myself as well as future members of the Gong laboratory will look back in gratitude for the seminal work that David has completed. I'd like to thank Senila Yasmin and Bea Fernandes for their kind welcome to the Gong laboratory and for devoting many hours to teaching me software and techniques. Thank you to Tate Valerio and Irving Zhao for their great work as giant vacuole tracers. I'd like to thank Sydney Holder for discovering a technique that greatly accelerated the time-consuming process of giant vacuole tracing. Thank you to Dr. Andrew Taylor for reading my thesis and offering positive criticism. Finally, I'd like to reiterate my thanks to Dr. Gong, who has been a wonderful mentor, teacher, and scientist.

.

**INVESTIGATION OF GIANT VACUOLES IN THE INNER WALL  
ENDOTHELIUM OF SCHLEMM'S CANAL AT PHYSIOLOGIC PRESSURE  
AND COMPARISON OF THE TYPES AND SIZE OF GIANT VACUOLES IN  
HUMAN EYES PERFUSED AT 7- AND 15-MM HG USING SERIAL BLOCK-  
FACE SCANNING ELECTRON MICROSCOPY**

**BENJAMIN L SOARES**

**ABSTRACT**

Glaucoma is a disease characterized by elevated intra-ocular pressure and chronic, irreversible loss of vision. The precise mechanism by which outflow resistance is generated remains elusive. We investigated a unique structure called the giant vacuole (GV) in the inner wall endothelium of Schlemm's canal (SC) that contribute to regulating outflow resistance. This study aimed to: 1) investigate the types and size of GVs in eyes perfused at 7 mmHg (physiological pressure in enucleated eyes) in the inner wall endothelium of SC using serial block-face scanning electron microscopy (SBF-SEM) and subsequent three-dimensional (3D) reconstruction of GVs; 2) to compare differences in the types and sizes of GVs in eyes perfused at 7 mmHg with published results in eyes perfused at 15 mm Hg (Swain et al, 2021). Two normal human donor eyes were perfused at 7 mmHg with fluorescent tracers to label the segmental outflow pattern followed by perfusion-fixation. Three radial wedges of tissue including SC from high-, low-, and non-flow areas of each eye based on tracer distribution were processed for SBF-SEM. GVs were counted and typed (Type I: no intracellular pore (I-pore), no basal opening, Type II: no I-pore, present basal opening, Type III: no basal opening, present I-pore, and Type IV:

present I-pore and basal opening). 3D reconstruction was performed on a GV subset. A subset of GVs was randomly selected for 3D reconstruction to measure GV volume. GVs in eyes perfused at 7 mmHg were compared with a previous GV study in eyes perfused at 15 mmHg. A similar number of images were analyzed at 7 mmHg (9586 images) and 15 mmHg (9802 images). Statistical analyses were performed using R statistical computing package.

There was a greater number of GVs at 15 mmHg (3302 GVs) compared to 7 mmHg (1312 GVs). Type IV GVs were more abundant in the high-flow than non-flow areas at both pressures ( $P \leq 0.01$ ). GVs with I-pores were significantly larger than GVs without I-pores in all flow-type areas at both pressures ( $P \leq 0.01$ ). GVs with I-pores were similar in volume at both pressures in all GVs and in high- and non-flow areas. However, GVs without I-pores were significantly larger in volume at elevated pressure ( $P \leq 0.01$ ). SBF-SEM and 3D reconstruction allowed for accurate identification of GV types and size. Comparing both pressures, the volume of GVs with I-pores were similar, while the volume of GVs without I-pores were larger at elevated pressures. This may indicate a threshold size of GVs for pore formation. GVs with I-pores were significantly larger than GVs without I-pores in all flow-type areas at both pressures suggesting that larger size of GVs is a contributing factor for GV-associated I-pore formation. More Type IV GVs observed in the high-flow areas at both pressures suggest that Type VI GV formation may play a role in regulating segmental outflow and increasing this type of GV may increase the total high-flow area.

## TABLE OF CONTENTS

DEDICATION.....	v
ACKNOWLEDGMENTS .....	vi
ABSTRACT.....	vii
TABLE OF CONTENTS.....	ix
LIST OF FIGURES . .....	xi
LIST OF ABBREVIATIONS.....	xii
CHAPTER ONE - Introduction .....	1
CHAPTER TWO – Methods, Results, and Discussion .....	13
BIBLIOGRAPHY.....	42
CURRICULUM VITAE.....	47

## LIST OF TABLES

Table 1 .....	23
Table 2 .....	23
Table 3 .....	24
Table 4 .....	25
Table 5 .....	27

## LIST OF FIGURES

Figure 1 .....	2
Figure 2 .....	4
Figure 3 .....	4
Figure 4 .....	5
Figure 5 .....	6
Figure 6 .....	6
Figure 7 .....	7
Figure 8 .....	11
Figure 9 .....	15
Figure 10 .....	17
Figure 11 .....	17
Figure 12 .....	19
Figure 13 .....	20
Figure 14 .....	28
Figure 15 .....	30
Figure 16 .....	32
Figure 17 .....	34
Figure 18 .....	39

## LIST OF ABBREVIATIONS

AH.....	Aqueous humor
CC .....	Collector channel
GV.....	Giant vacuole
IOP .....	Intra-ocular pressure
IW .....	Inner wall (endothelium of Schlemm's canal)
JCT .....	Juxtacanalicular connective tissue
POAG.....	Primary open angle glaucoma
SBF-SEM.....	Serial block-face scanning electron microscopy
SC.....	Schlemm's canal
TM.....	Trabecular meshwork

## **CHAPTER ONE - Introduction**

### **Overview of Glaucoma**

Glaucoma is the second leading cause of blindness after cataracts, with an estimated 57.5 million people worldwide affected by primary open-angle glaucoma in 2018 (Allison et al., 2020). By 2040 the number of people suffering from this condition is expected to reach approximately 111.8 million (Tham et al., 2014). There are distinct subtypes of glaucoma, including open angle and closed angle glaucoma and secondary glaucoma. However, primary open angle glaucoma (POAG) accounts for approximately 74% of glaucoma cases (Kapetanakis et al., 2016). POAG refers to a glaucoma in which the iridocorneal angle is open and there is no identifiable secondary cause of elevated intraocular pressure (IOP). IOP is maintained within a normal range through a dynamic balance between the production and drainage of aqueous humor (AH) in the eye. The primary risk factor for the development and progression of POAG is elevated IOP, resulting from increased outflow resistance. A chronic loss of function in the aqueous humor drainage pathways causes elevation of IOP, damage to the optic nerve, and gradual, irreversible loss of vision.

#### **The conventional aqueous humor outflow pathway**

AH is produced in the ciliary body. There are two main pathways through which AH exits the anterior chamber of the eye. The conventional, or trabecular outflow pathway is the pathway through which the majority of AH exits the eye and will be the focus of the present investigation (Chaum & Freddo, 2017). AH passes from the anterior chamber into Schlemm's Canal (SC) through the trabecular meshwork (TM), before entering collector

channels, the deep scleral plexus, the intrascleral plexus, and finally episcleral veins (Fig. 1). Pressure-induced changes to the dimensions of SC appear to directly affect outflow facility (Chen et al., 2020). The majority of resistance that AH encounters along the conventional outflow pathway is thought to be localized to the juxtacanalicular connective tissue (JCT) region of the TM and the inner wall (IW) endothelium of SC, while 30-50% of the resistance is thought to occur distally to SC (Ethier, 2002; Ethier et al., 1995; Mäepea & Bill, 1989). The pores and giant vacuoles (GVs) of the endothelium of SC are thought to significantly contribute to the modulation of the aqueous humor outflow resistance (Chen et al., 2020; Ethier et al., 1986).

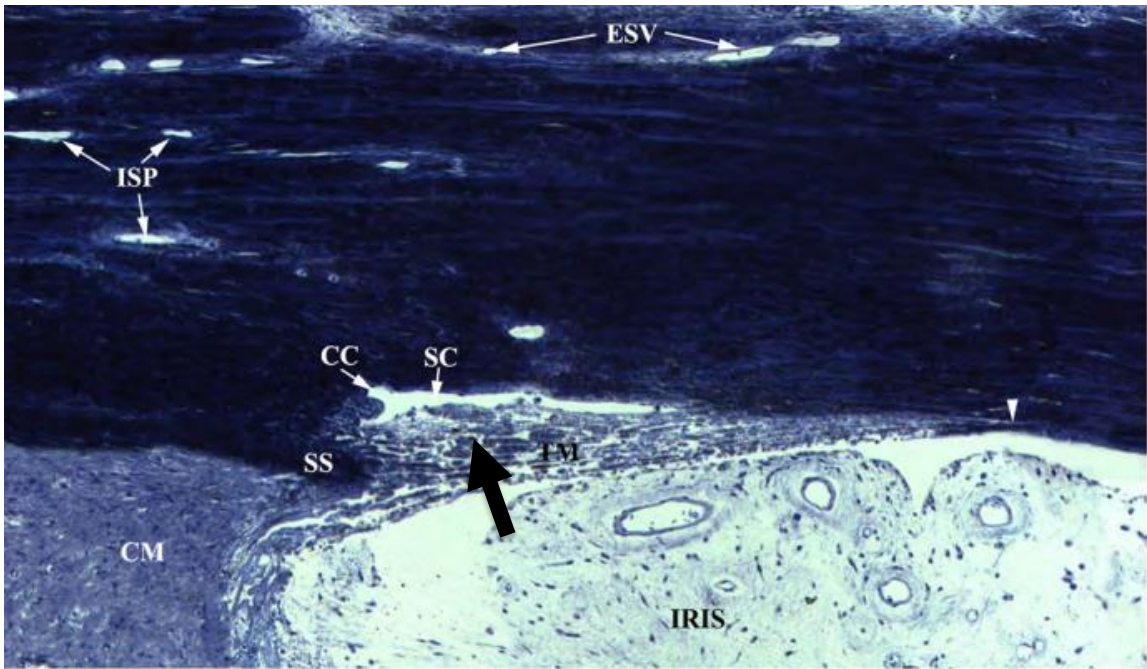


**Figure 1.** Conventional outflow pathway. Light micrograph of meridional section showing the anterior chamber angle. Aqueous humor passes through the trabecular meshwork (TM), into Schlemm's canal (SC), then collector channels (CC), and the intrascleral plexus (ISP), before draining into episcleral veins and leaving the eye. The iris, ciliary muscle (CM), scleral spur (SS) and the terminus of Descemet's membrane, also known as Schwalbe's line (white arrowhead) are also shown. Direction of aqueous humor movement across the TM is shown by the black arrow. Adapted from (Gong and Swain., 2020).

### **The inner wall endothelium of Schlemm's Canal**

The inner wall (IW) endothelium of SC is a unique anatomic structure important for AH drainage. The IW of SC is a monolayer of endothelial cells connected by tight junctions (Figs. 2, 3). From the TM, AH must pass through this monolayer to enter SC. There are two routes: a transcellular route via pores (I-pores), and a paracellular route via pores between two neighboring cells (B-pores) (Fig. 4). When AH moves through an intracellular pore, this pore can either be associated with an intracytoplasmic giant vacuole or not. GVs and I-pores are the focus of the present study. The process of vacuolation and transcellular pore formation has been studied in detail, and a model diagramming this cycle was initially proposed by Tripathi (Tripathi & Tripathi, 1974) (Fig.5). Initially, the membrane indents as aqueous humor presses against the basal aspect of the endothelial cell. The basal membrane may reform and give the GV the appearance of a small intracellular void. Alternatively, AH can continue to press against the basal aspect of the cell to form a basal opening. The cellular lining thins as more AH enters the GV and increases its volume. As the cellular lining continues to thin and the GV expands in volume, a pore may form apically and allow transcellular movement of AH. Eventually, the basal opening and/or pore can close, and the cell returns to its unvacuolated state. In fixated tissue, GVs have been categorized as four types based on their vacuolation cycle stage; Type I: no intracellular pore (I-pore), no basal opening, Type II: no I-pore, present basal opening, Type III: no basal opening, present I-pore, and Type IV: present I-pore and basal opening (Grierson & Lee, 1978; Koudouna et al., 2019).

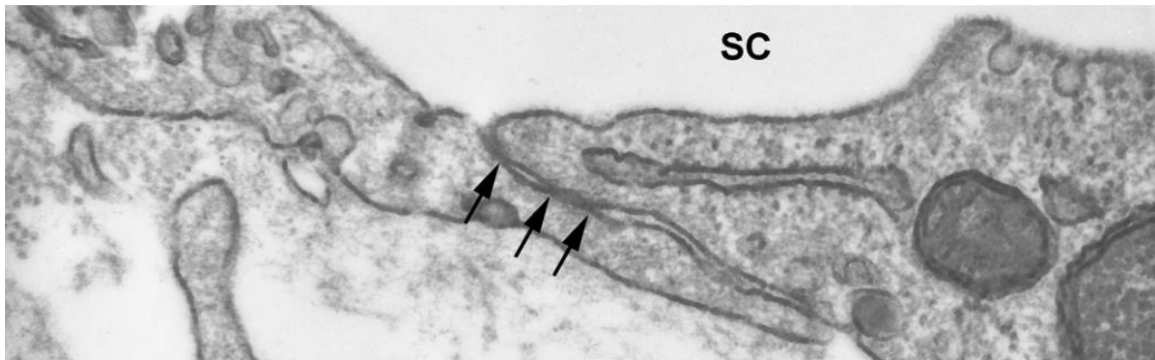


**Figure 2. Tight junctions between inner wall (IW) endothelial cells.** Tight junctions between adjacent IW endothelial cells (black arrows) form the cellular monolayer that separates the juxtacanalicular tissue from Schlemm's canal (SC) (From Gong & Swain, 2020).

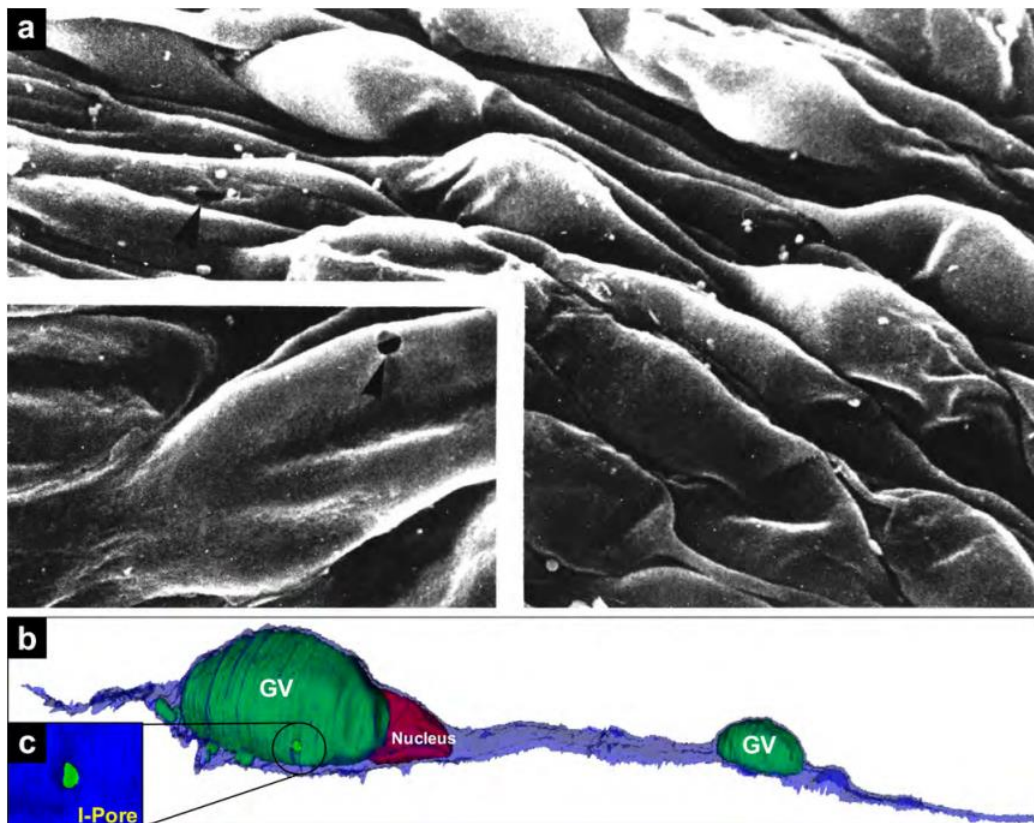


**Figure 3. Inner wall (IW) endothelial cells of Schlemm's canal (SC).** A: A scanning electron micrograph of the luminal surface of the IW of SC, showing giant vacuoles (GVs) that appear as bulges and a GV associated I-pore (arrowheads). In the inset, a magnified GV associated I-pore is shown. B: 3D reconstruction of an inner wall endothelial cell with GV (green) and a nucleus (red). Cell membrane is shown in blue. C: Magnified view of a GV-associated I-pore shown in the 3D reconstruction (From Lai et al., 2019).

*Segmental outflow around the circumference of Schlemm's canal*

The outflow of AH around the circumference of SC is not uniform, but segmental (Cha et al., 2016; Swaminathan et al., 2014). Some regions experience active flow while others are relatively inactive. At any given time, only a fraction of the outflow pathway is actively involved in aqueous humor drainage (Gong & Swain, 2020). Cha and colleagues found variation in active outflow patterns around the circumference of SC manifesting as different effective filtration areas and fluorescent tracer distributions (Fig.6). An increased concentration of fluorescent tracer was observed in the TM near collector channels (CC) (Cha et al., 2016). Additionally, the TM and JCT in active flow regions appear more expanded with greater areas of empty space (Fig. 7).

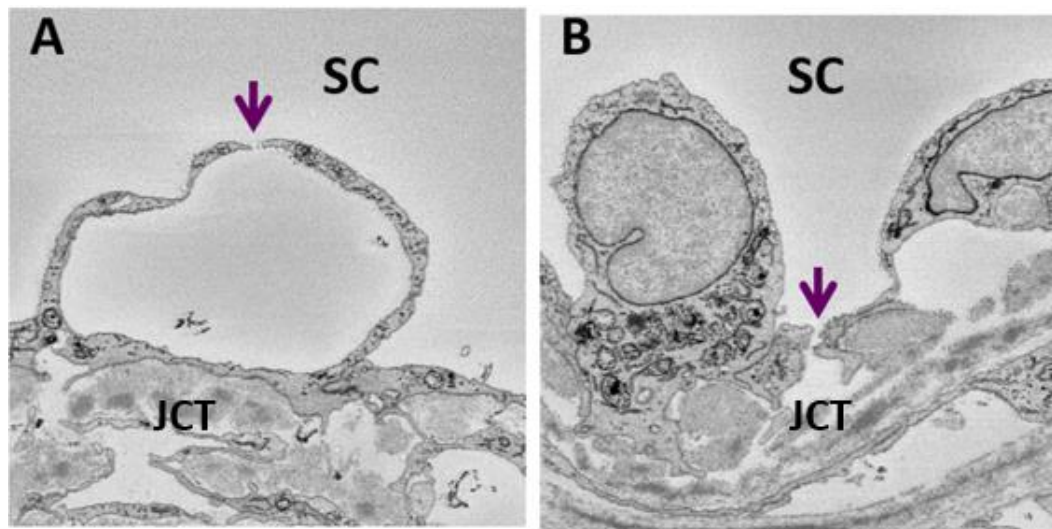


**Figure 4. Examples of GV associated I-pore (A) and B-pore (B).** A: GV-associated I-pore is indicated by an arrow and allows aqueous humor (AH) to move from the juxtacanalicular connective tissue (JCT) into Schlemm's canal (SC). B: B-pore forms intercellularly between two inner wall endothelial cells and is an alternative route for AH to cross from the JCT into SC (From Le et al., 2019).

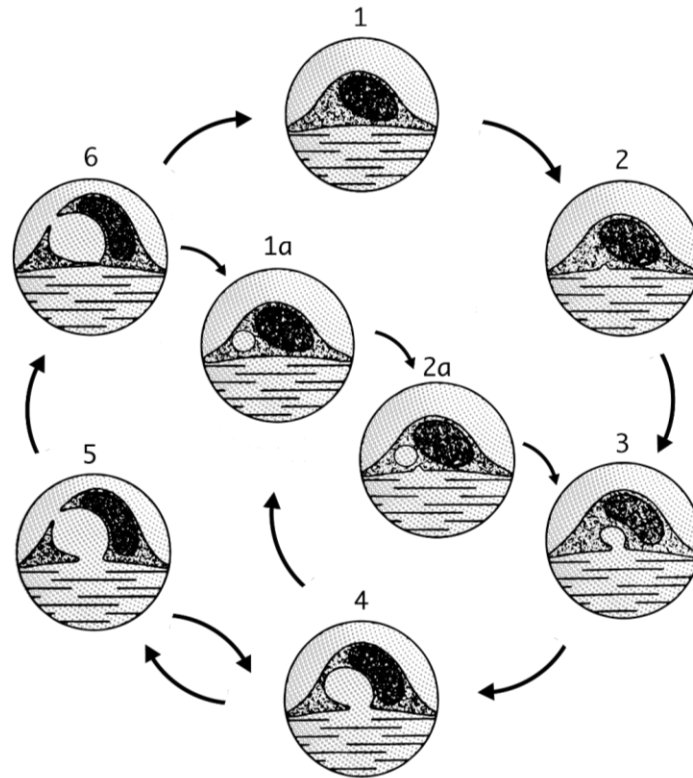


**Figure 5. Vacuolation cycle diagram proposed by Tripathi and modified by Swain.** (1) Un-vacuolated inner wall (IW) endothelial cell. (2) An indentation is formed when aqueous humor (AH) presses on the basal aspect of the IW cell, forming a basal opening. (3) The giant vacuole (GV) continues to enlarge as AH enters the basal opening. (4) Continued enlargement of the GV. (5) An I-pore may form apically allowing for transcellular movement of AH. The membrane of the GV can then close apically, returning the vacuole to stage 4, or basally, in which the vacuolation cycle proceeds to stage 6. (6) The basal membrane of the IW cell reforms leaving the apical I-pore open. (1a) An intermediate stage in the vacuolation cycle in which the basal membrane of the GV reforms, enclosing a small amount of AH intracellularly. (2a) A second basal indentation may appear, and this basal opening may connect with the intracellular GV (From Swain, 2021).

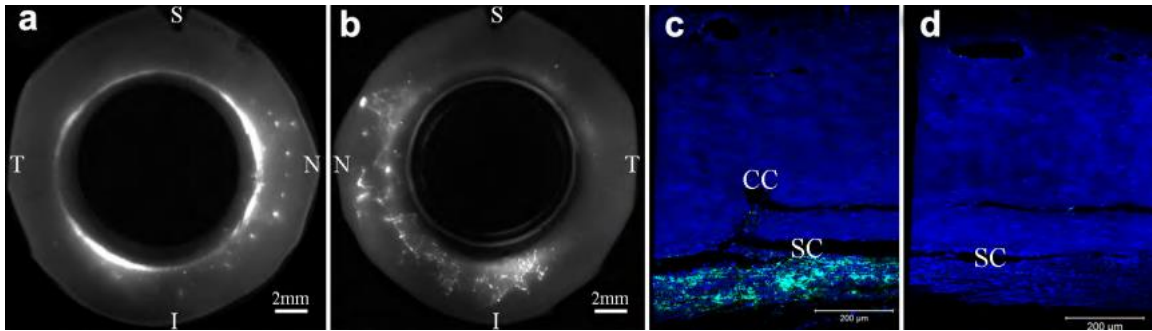


**Figure 6. Segmental outflow pattern visualized with fluorescent tracers.** A: Poserior view of tracer distribution in trabecular meshwork (TM). Brighter areas contain more active outflow. S – Superior, N – Nasal, I – Inferior, T – Temporal. B: Anterior view of tracer distribution in the scleral veins. C: Confocal microscopic image of abundant tracer distribution (green) in Schlemm's canal (SC) near a collector channel (CC). D: Confocal microscopic image showing absence of tracers in a region of inactive flow (From Gong & Francis, 2014).

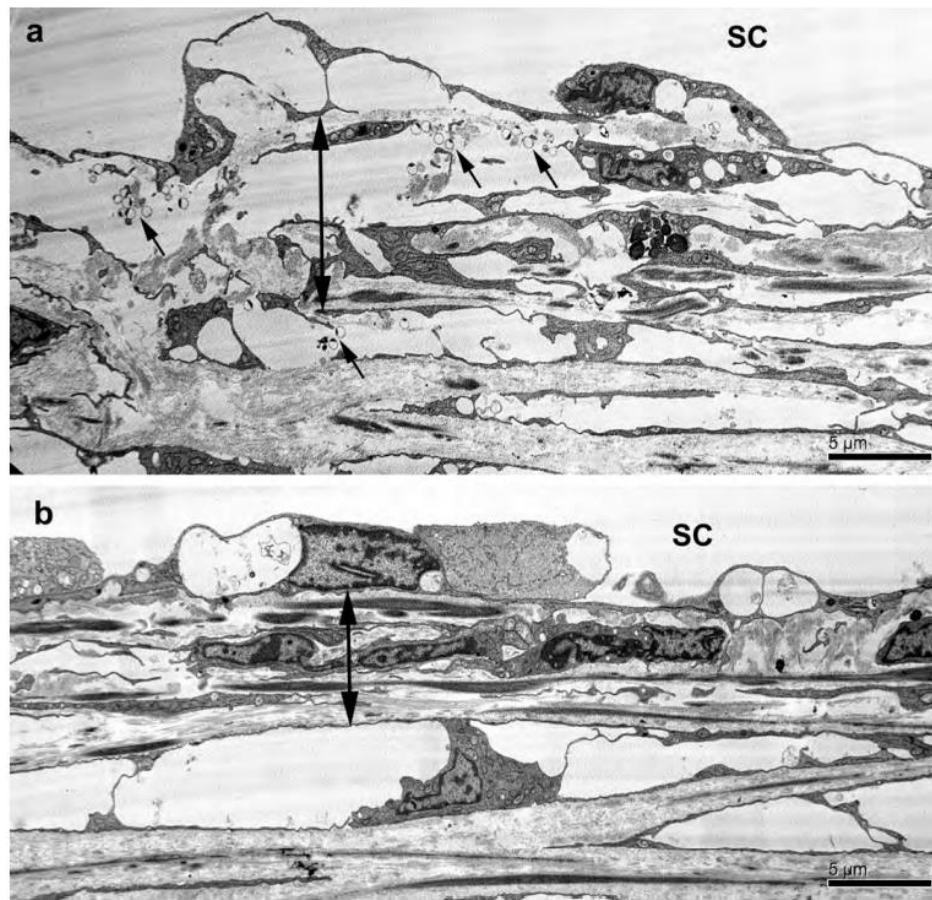


**Figure 7. Juxtacannalicular tissue (JCT) and trabecular meshwork (TM) expansion in regions of active flow.** A: An area of active outflow with expanded TM and JCT (double arrow). Tracers are more readily observed in the area of active outflow (arrows). B: An area without active outflow, with less expanded TM and JCT and a lack of observable tracers (From Gong & Swain, 2020).

### **GVs and pores in glaucomatous eyes**

Upon examination with scanning electron microscopy, Allingham et al. discovered that pores were less common in glaucomatous eyes compared to normal eyes (Allingham et al., 1992). Their study observed an increased flow resistance at the IW in glaucomatous eyes associated with decreased pore formation, leading them to the conclusion that the IW endothelium in glaucomatous eyes appears to be more resistant to pore formation. Their study discusses the limitations of scanning electron microscopy, and the need for a more comprehensive three-dimensional imaging technique that can distinguish between GVs and IW cell nuclei. Another study by Johnson et al. confirmed decreased pore formation in glaucomatous eyes (Johnson et al., 1992). Johnson and colleagues observed a density of 835 pores/mm<sup>2</sup> in normal eyes and 160 pores/mm<sup>2</sup> in glaucomatous eyes, suggesting an approximately fivefold lower outflow facility in glaucomatous eyes.

### **GV morphology with increasing IOP**

Previous studies have examined the relationship between increasing IOP and changes in GV morphology and number.

In their 1977 study, Grierson & Lee investigated GV morphology and number as a function of IOP in vivo rhesus monkey eyes using light microscopy (Grierson & Lee, 1977, 1978). They prepared four blocks of tissue from each quadrant of the eye, with each block cut into one hundred 1.5  $\mu\text{m}$  sections for light microscopy. Every tenth section was used for a vacuole count. GVs were counted in the following regions of the endothelium of SC: (1) the trabecular aspect, (2) the corneoscleral aspect, and (3) the

septae and the endothelium connecting the trabecular and corneoscleral aspects of SC. The GV count was extrapolated to a mean GV count per section. Grierson and Lee observed an approximately linear relationship between GV number and IOP from 8 to 30 mmHg, and then a decreased number of GVs from 30 to 50 mmHg. Additionally, they observed a complete absence of GVs at 0 mmHg. Vacuolar length was assessed by observing the total number of 1.5  $\mu\text{m}$  sections that a vacuole appeared on, and vacuolar volume was estimated by assuming a regular spheroid shape and evaluating using the vacuolar length estimation described above and the maximum cross-sectional vacuolar width. Grierson and Lee noticed a significant increase in vacuolar volume with increasing pressure from 8 to 30 mmHg, and described the relationship between volume and IOP as exponential.

In their study on GV biomechanics, Pedrigi et. al used confocal microscopy and an in vitro model system employing seeded human SC endothelial cells (Pedrigi et al., 2011). They noticed what appeared to be an increased number of giant vacuole-like structures with increased pressure). Additionally, they observed significant increases in GV dimensions (length, width and height) as perfusion pressure was increased.

Lai et al. used serial block-face scanning electron microscopy (SBF-SEM) imaging to examine IW cell morphology and connections between IW cells and IW cells/ JCT cells. Lai and colleagues compared the 3D reconstructed IW cells of SC between perfusion- (15 mm Hg) and immersion-fixed (0 mm Hg) eyes (Lai et al., 2019). They found that

summed GV volume per cell increased in perfusion-fixed eyes compared to immersion-fixed eyes. Lai and colleagues note a need to investigate factors that may influence GV volume, including active and inactive flow regions and perfusion pressure. Additionally, they found that there were fewer IW/JCT cell connections in perfusion-fixed eyes compared to immersion-fixed eyes.

Swain and colleagues investigated giant vacuole morphology of IW endothelial cells of SC in high-, low- and non-flow areas of enucleated human eyes perfused at 15 mm Hg using SBF-SEM imaging. They found a greater number of GVs containing I-pores in high-flow areas, and that GVs with I-pores were greater in size than GVs without. Swain and colleagues' findings suggest that the larger size of GVs may contribute to the formation of I-pores. They note a need to assess GV morphology at different perfusion pressures.

### **Advantages of Serial Block-Face Scanning Electron Microscopy and 3D reconstruction**

SBF-SEM- provides high-resolution three-dimensional (3D) images from small blocks of tissue. The technique utilizes an ultramicrotome and scanning electron microscope in conjunction to generate a series of images in perfect alignment, allowing for the digital reconstruction of sub-cellular structures. In our investigation, sub-cellular structures were identified on a series of sections and then manually traced, and the traces were then digitally reconstructed to create 3D volumes (Fig. 8). The comprehensive 3D visualization that SBF-SEM provides is particularly useful when studying GVs, where alterations in shape and volume may correspond to alterations in organelle function. Most

previous studies on GV morphology have used light microscopy or scanning electron microscopy, which do not allow for the detailed 3D visualization that SBF-SEM provides.

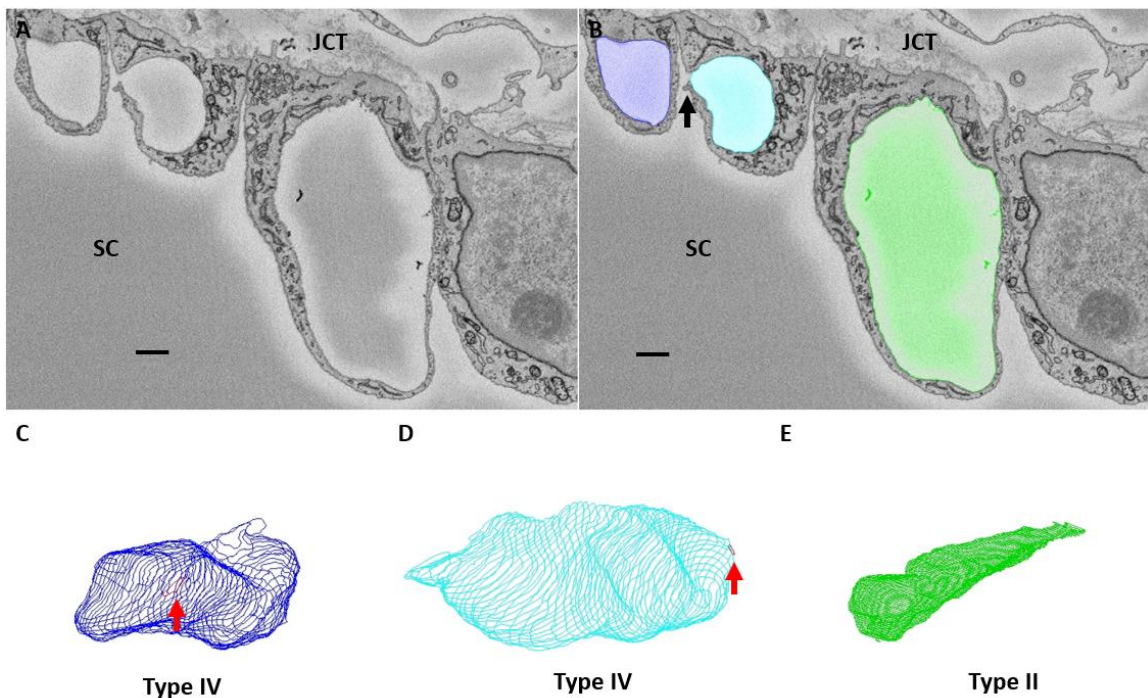


**Figure 8. 3D Giant Vacuole (GV) Reconstruction.** A: Three adjacent GV's with Schlemm's canal (SC) and the juxtacanalicular connective tissue (JCT) region labeled. B: Traces of each GV on one section. Black arrow indicates an I-pore on the side of the blue traced GV. C: 3D reconstruction of the blue GV after digital combination of aligned traces. The GV is a Type IV GV (GV has an I-pore and a basal opening). D: 3D reconstruction of the teal GV. The GV is a Type IV GV. E: 3D reconstruction of green GV. The GV is a Type II GV (GV has a basal opening but no I-pore). Scale bar = 1  $\mu$ m.

Light microscopy does not offer enough resolving power to image smaller GV's and pores, and single-section electron microscopy, while able to provide superior resolution, does not allow for visualization of the three-dimensional structure of a GV. SBF-SEM allows us to investigate the fine details of GV morphology. In this study, we investigated GV size, type, and number at physiologic pressure and then compared the morphologic

factors at physiologic with those at elevated pressure using SBF-SEM imaging. By studying pressure related changes in the micro-anatomy of the inner wall endothelial cells of SC, we hope to gain better understanding of GV and pore formation with increasing IOP, which is a primary risk factor in development and progression of primary open angle glaucoma.

### **Study Objectives**

The aims of this study are:

- 1) To investigate the types and size of Schlemm's canal (SC) inner wall endothelium giant vacuoles (GVs) in eyes perfused at physiological pressure of 7 mmHg, using serial block-face scanning electron microscopy (SBF-SEM) and subsequent three-dimensional (3D) reconstruction of GV's.
- 2) To compare differences in the types and sizes of GV's in eyes perfused at 7 mmHg with previous GV studies in eyes perfused at an elevated pressure of 15 mmHg (Swain et al, 2021).

## **CHAPTER TWO – Methods, Results, and Discussion**

### **Materials & Methods**

#### **Human donor eyes**

This study used two pairs of human eyes (Eye 1: 66-years-old; Eye 2: 55-years-old; without traceable identity or any known ocular diseases (Eye 1: NDRI Philadelphia, PA. Eye 2: Lions VisionGift Portland, OR.) The eyes were received within 24 hours postmortem. The eyes were then inspected under dissecting microscope for any gross damage and were managed in accordance with the Boston University Medical Center Institutional Review Board and the guidelines outlined in the Declaration of Helsinki concerning the use of human tissues.

#### **Ocular perfusion and fixation**

The following methods for ocular perfusion, global imaging, and serial block-face imaging were first described in Swain's study on GVs at 15 mmHg (Swain et al., 2021). Ocular perfusion was carried out using a previously established protocol (Scott et al., 2009). First, eyes were perfused with pressure-controlled hydraulic pumps using Dulbecco's phosphate-buffered saline (pH 7.3; Invitrogen, Grand Island, NY, USA) with 5.5 mM D-glucose (collectively referred as GPBS) for 30 minutes to establish a stable baseline facility at constant pressure of 7 mmHg. Fluids in the anterior chamber of the eyes were then exchanged and perfused with a fixed volume (200  $\mu$ L; 1:1000 dilution in GPBS) of red fluorescent tracers (size: 200 nm; catalog number: F8810; Thermo Fisher

Scientific, Waltham, MA, USA) to label the outflow pattern. Then, perfusion-fixation with modified Karnovsky's fixative (2.5% glutaraldehyde and 2% para-formaldehyde in 0.1-M sodium phosphate buffer; pH = 7.3) was carried out for 30 minutes. A small incision (~5 mm) was made along the equator. Finally, eyes were immersed in fixative as previously described overnight.

### **Global imaging and tissue dissection**

Global imaging was performed to visualize the segmental outflow using a previously established protocol (Cha et al., 2016). The globe of each eye was hemisected into posterior and anterior segments. Excess conjunctiva, vitreous, cornea, ciliary body, and the iris were then removed. En face imaging of anterior segments on episcleral and TM surfaces was completed with a 300 mm lens on a 4000 MP VersaDock imaging system (Bio-Rad Laboratories, Hercules, CA, USA) for 5 seconds. Quantity One (Bio-Rad) software was used in image production.

Guided by global images as previously described (Swain et al., 2021), tissue wedges (2 x 2 x 2 mm) of the TM, including SC and a small piece of sclera were dissected from the following flow-type areas: high- low-, and non-flow (Fig. 9) from each eye (total: 6 wedges). The classification of flow-type areas was based on the visual observation of the amount of fluorescence on TM and episcleral surfaces. High-flow areas had bright fluorescence on both anterior (episcleral veins) and posterior (TM) sides, while low-flow areas had intermediate fluorescence and non-flow areas had no visible fluorescence.

Tracer numbers were estimated in each block as described in the following section on serial block-face scanning electron microscopy.

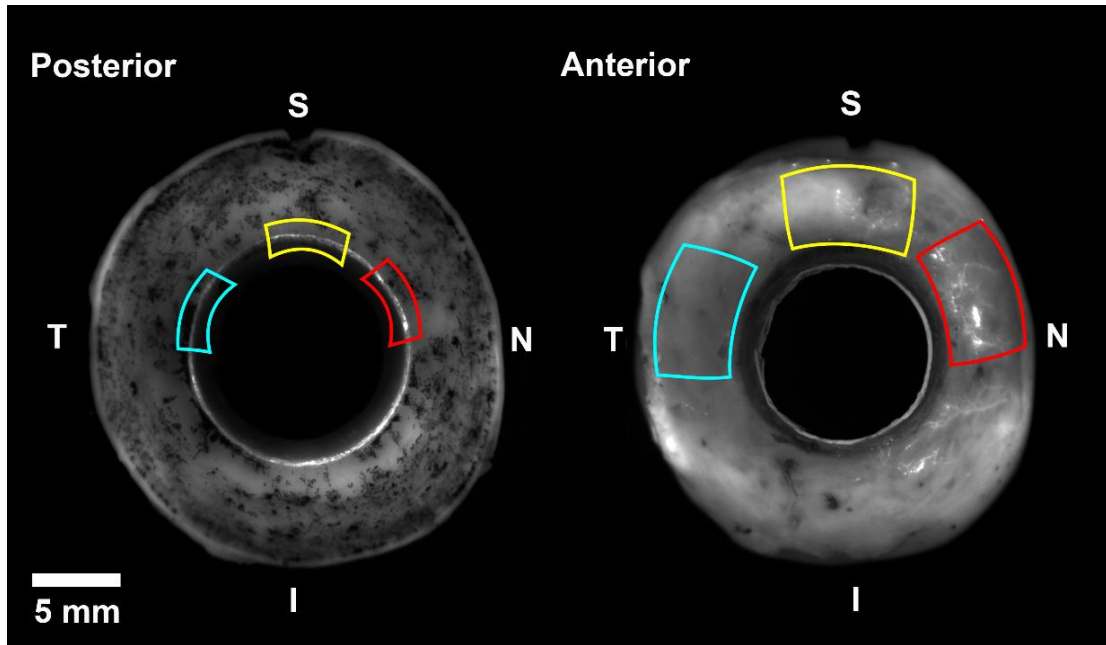


**Figure 9. Global imaging of fluorescent tracer distribution in three flow-type areas.** Flow-type areas were classified and dissected for serial-block face scanning electron microscopy according to fluorescent tracer distributions. High-flow area (*red*) had bright fluorescence on both the posterior (trabecular meshwork) and anterior (episcleral veins) sides. Low-flow areas (*yellow*) had intermediate fluorescence on both sides. Non-flow areas (*blue*) had no visible fluorescence on either side. I = inferior; N = nasal; S = superior, T = temporal. (From Swain et al, 2021).

### Serial block-face scanning electron microscopy

Tissue sections were processed and embedded into Epon blocks by an SBF-SEM technician at the Cleveland Clinic (Cleveland, OH), according to an established technique (Deerinck et al., 2010). Wedges of tissue were post-fixed with thiocarbohydrazide and OsO<sub>4</sub>/K ferrocyanide, before en-bloc staining with lead aspartate and uranyl acetate. Tissues were dehydrated with a series of ascending ethanol concentration and embedded in Epon resin. The regions of interest (including TM, SC, and a small portion of sclera )

in each block were imaged using a Zeiss Sigma VP serial block-face scanning electron microscope equipped with a Gatan 3View (Gatan, Inc., Pleasanton, CA, USA) in-chamber ultramicrotome stage and low-kV backscattered electron detectors that were optimized for 3View systems. Following the capture of each image, an automated ultramicrotome cut another section and the image capturing process was completed until the entire block was processed. The size of each two-dimensional pixel on each image was  $0.0101 \mu\text{m} \times 0.0101 \mu\text{m}$ , and each section was  $0.13 \mu\text{m}$  thick. Images were compiled and aligned for analysis.

Images were visualized using Reconstruct (Fiala, 2005). 9586 images were screened. To confirm flow-type areas, tracers, were labeled and counted every 50 sections using the Reconstruct stamp tool, and then the mean tracer number per section was determined (Eye 1: High-flow – 30 t/s, low-flow – 21 t/s, non-flow – 19 t/s. Eye 2: High-flow – 34 t/s, low-flow – 4 t/s, non-flow – 1 t/s) (Fig. 11).

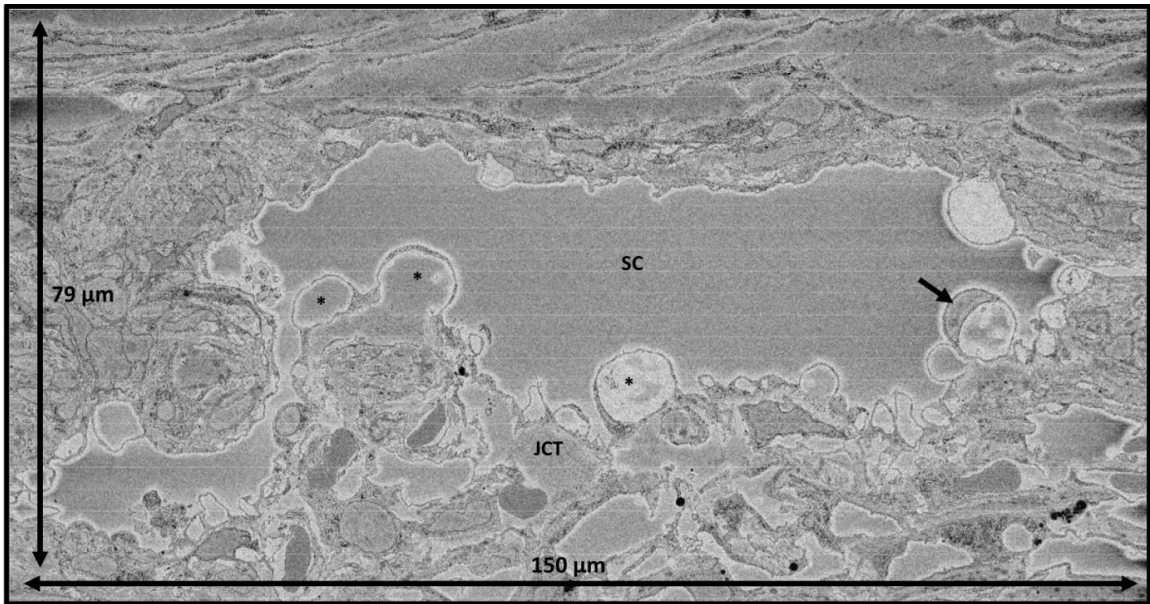


**Figure 10. Full imaging field of one section (150  $\mu\text{m}$  x 79  $\mu\text{m}$ ) from a high-flow region of an eye perfused at 7 mmHg.** Schlemm's Canal (SC) is visible, along with inner wall cell nuclei (arrow) and giant vacuoles (\*). Adjacent to the inner wall endothelial cells is the juxtacanalicular connective tissue (JCT) region.

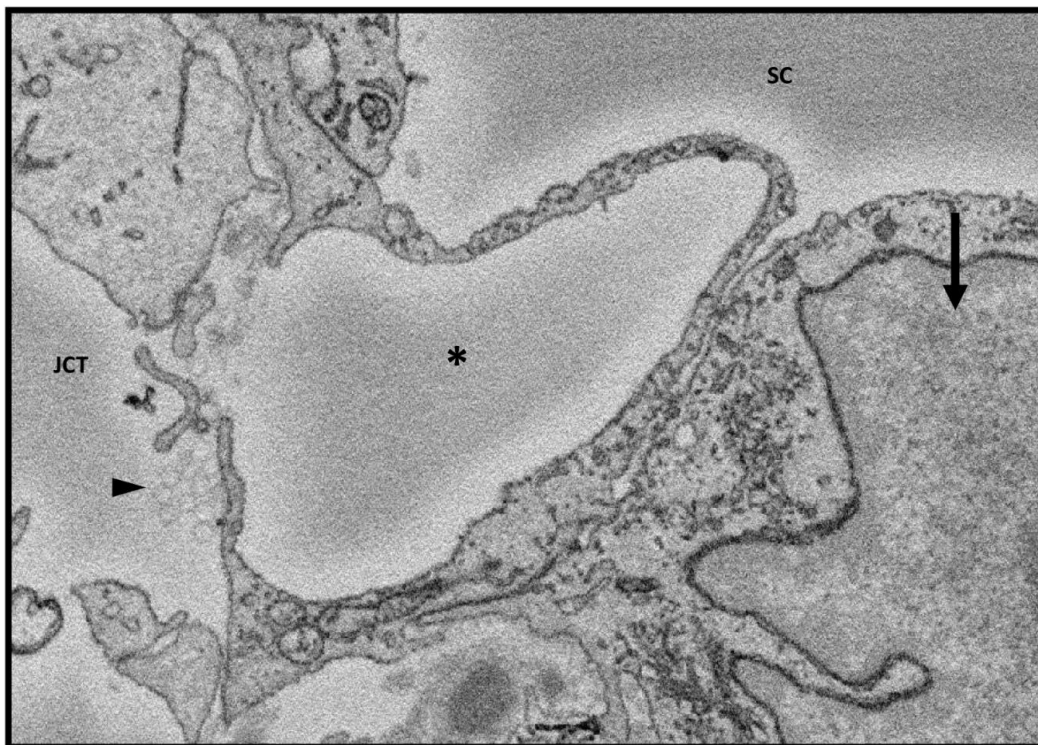


**Figure 11. Tracers near the basal opening of a giant vacuole in a high-flow region.** The inner wall endothelial lining cells of Schlemm's Canal (SC) with giant vacuole (\*) and nucleus (arrow) and the underlying juxtacanalicular connective tissue (JCT) region can be seen. Tracers (arrowhead) were seen near the basal opening of a giant vacuole (\*).

**Giant vacuole marking**

GVs that extended out of the margins of the image were excluded from labeling. Two investigators individually determined whether GVs had basal openings and I-pores.

Openings in the cellular lining were determined to be I-pores if they were characterized by smooth borders and clear separation, and openings that appeared artifactual with rough borders were excluded on the grounds that they may have resulted from damage during the sectioning process. GV type was assigned based on previous studies: Type I: no intracellular pore (I-pore), no basal opening, Type II: no I-pore, present basal opening, Type III: no basal opening, present I-pore, and Type IV: present I-pore and basal opening (Grierson and Lee, 1978; Koudouna et al, 2019) (Fig. 12). GV size was estimated through recording the number of sections that a GV appeared in, and median GV spans were compared between GVs with and without I-pores in each flow-type area and overall, and GV types were also compared in this manner.

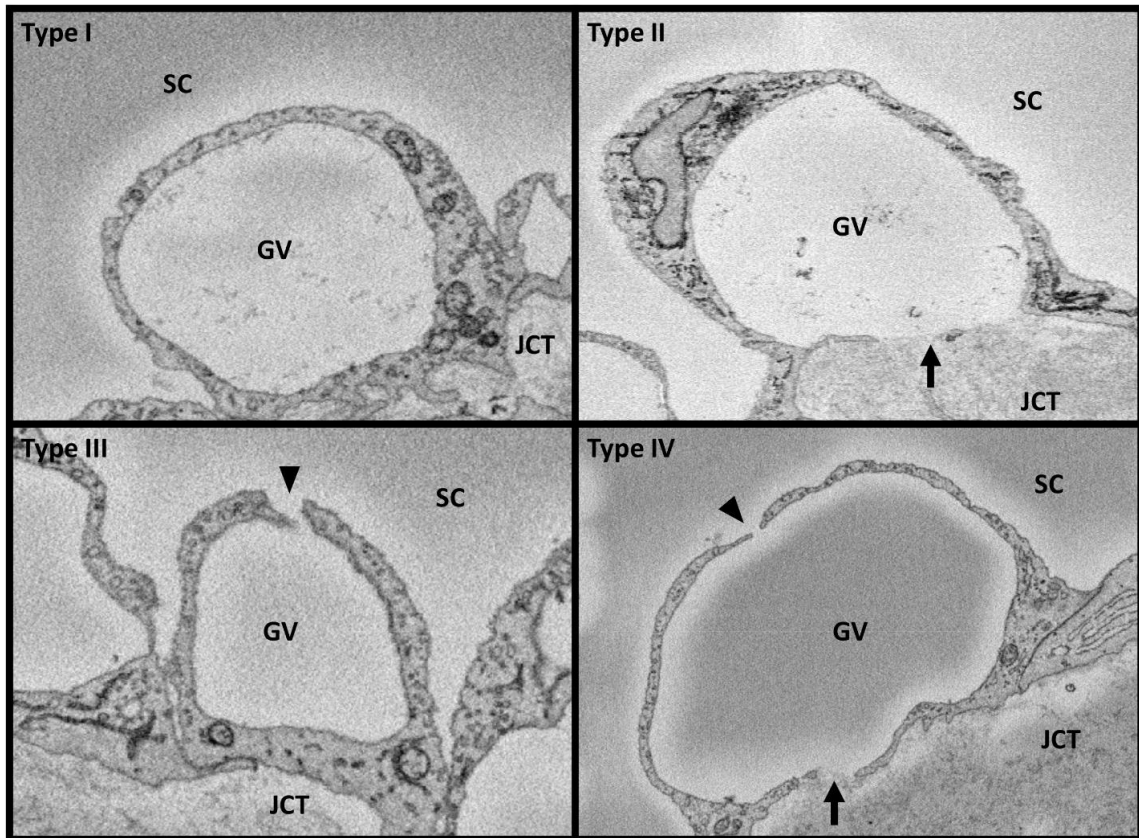


**Figure 12. Examples of each giant vacuole (GV) type.** GVs of endothelium of Schlemm's canal (SC) were categorized into types based on the presence of basal openings and/or meshwork pores. Type I GVs have neither basal opening nor I- pore. Type II GVs have basal opening (arrow) and no apical I- pore. Type III GVs have no basal opening but have an I- pore (arrowhead). Type IV GVs have both basal opening and I-pore. The juxtacanalicular connective tissue (JCT) region can be seen in each example.

From a total 1312 GVs, a subset of GVs (n= 300) that were completely within the imaging field with I-pores (n= 101) and without I-pores (n=199) were traced and reconstructed in 3D using Reconstruct software for evaluation of GV volume (Fig. 13). From eye 1, 21 GVs with I-pores were selected, and 77 GVs without I-pores were selected. From eye 2, 80 GVs with I-pores were selected, and 122 GVs without I-pores were selected. 300 GVs were determined to satisfy the sample size requirement at a confidence interval of 5 and confidence level of 95% for a population of 1312 GVs. In

each eye, all GVs with I-pores were selected for reconstruction and the remainder of GVs without pores (Type I and II GVs) were randomly selected. Each type I and II GV was assigned a number and a random number generator was used for selection. GVs were excluded if their volumes were less than  $1 \mu\text{m}^3$  to avoid including pinocytotic vesicles.

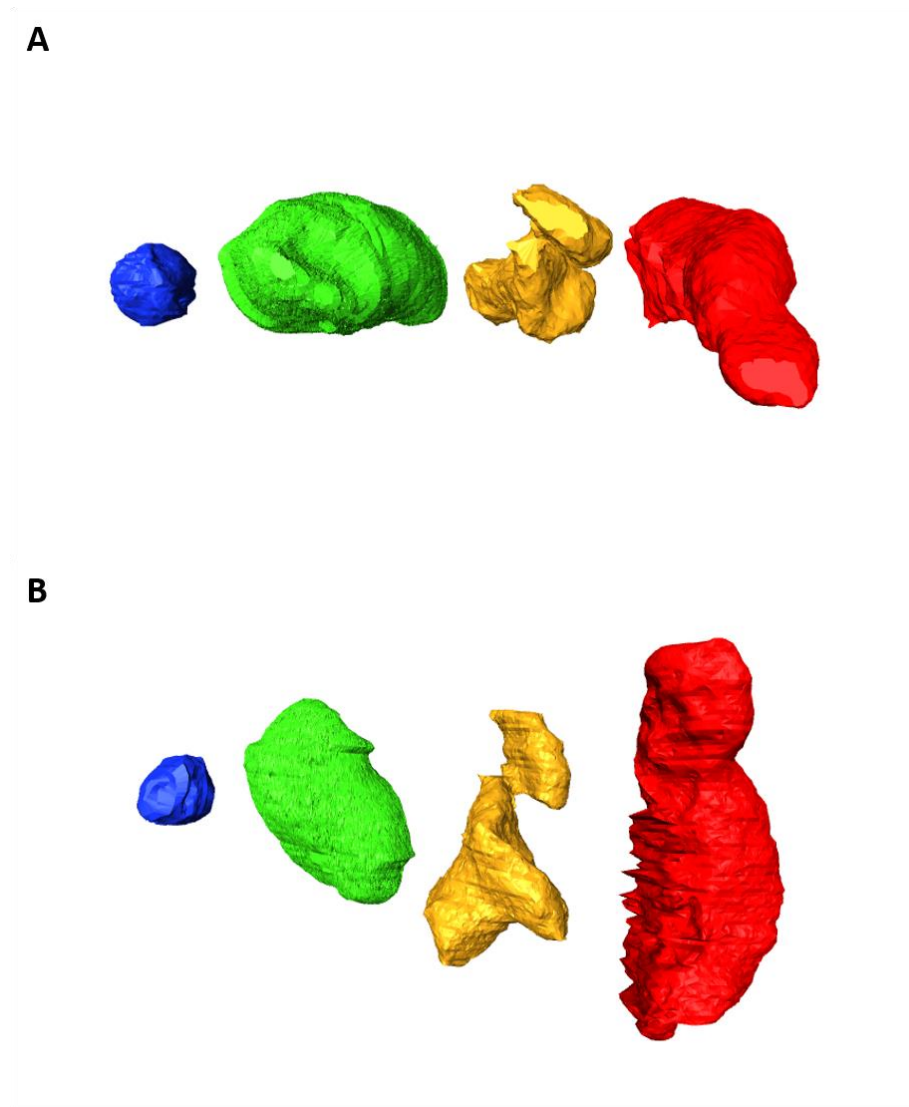


**Figure 13** Examples of interior volumes of each type of giant vacuole (GV) A: Frontal view of a Type I GV (blue), Type II GV (green), Type III GV (orange), and Type IV GV (Red). B: Superior view.

### **Comparison of GV types and size at 7 mmHg with data from a previous study at 15 mmHg.**

A comparison of the GV types and size between 7 and 15 mmHg was made. GV data at 15mmHg was collected in the present study with nearly identical methods of eye preparation and imaging (Swain et al., 2021). In the study at 15 mmHg, similarly, two eyes and 6 tissue blocks were used, with two blocks from each flow-type area. 3302 GVs from 9802 images were analyzed. A subset of GVs ( $n = 180$ ) that were completely within the imaging field with I-pores ( $n = 90$ ) and without I-pores ( $n = 90$ ) were traced manually and reconstructed in 3D. From eye 1, 45 GVs with I-pores were selected, and 45 GVs without I-pores were selected. From eye 2, 45 GVs with I-pores were selected and 45 GVs without I-pores were selected. The sampling distribution differed at 7 versus 15 mmHg because at 7 mmHg there were much fewer GVs with I-pores, so all GVs with I-pores were selected for tracing with the remainder of GVs randomly selected from the population of GVs without I-pores in order to satisfy an adequate sample size. At 15 mmHg however, all GVs were randomly selected. Each GV was assigned a number, and a random number generator was used to randomly select GVs for tracing.

Reconstruct was used to calculate GV volume. Each GV was traced on every section that it appeared, and the surface area of these traces was then used to calculate GV volume. GV volumes were compared between GVs with and without I-pores, and between GV types I – IV.

## Statistical methods

Statistical analyses were performed using R statistical computing package (version 4.1.3). A chi-square test was used to compare GV type distributions in different flow type areas and at different pressures. Kolmogorov-Smirnoff (KS) tests were used to test for normality of distributions. Non-normal distributions were reported by KS test in GV span, volume, and maximal CSA (all  $P < 0.01$ ) therefore, we chose to use non-parametric Kruskal-Wallis tests with post-hoc pairwise Wilcoxon rank-sum tests to test statistical significance

## Results

### GVs at physiologic pressure

#### *GVs with and without I-pores across flow-type areas*

Over 9586 images, 1312 GVs were observed. The flow-type area with the greatest number of GVs was non-flow (N = 681, over an area of .0786 mm<sup>2</sup>), followed by high-flow (N = 433, over an area of .0669 mm<sup>2</sup>) and low-flow (N = 196, over an area of .0548 mm<sup>2</sup>) (Table 1). The flow-type area with the highest percentage of GVs with I-pores was high-flow, with 15.9% of GVs containing I-pores (N = 69). The flow-type area with the highest percentage of GVs without I-pores was non-flow, with 95.6% of GVs not containing I-pores (N = 651) (Table 2). The overall percentage of GVs with I-pores was significantly different among flow-type areas (Chi-square test  $\chi^2 = 45.29$ ,  $P \leq 0.01$ ).

Flow-type area	Eye 1	Eye 2
High	.0348 mm <sup>2</sup>	.0321 mm <sup>2</sup>
Low	.0246 mm <sup>2</sup>	.0302 mm <sup>2</sup>
Non	.0412 mm <sup>2</sup>	.0374 mm <sup>2</sup>

**Table 1. Inner wall of Schlemm's canal (SC) surface area observed in each flow-type area and eye.** SC area was measured by tracing the inner wall endothelium every 50 sections, then multiplying the trace by 50 and summing across the entire block.

Flow-Type Area	GVs with I-pores	GVs without I-pores	Total
High	69 (15.9%)	364 (84.0%)	433
Low	14 (7.1%)	182 (92.9%)	196
Non	32 (4.7%)	651 (95.6%)	681

**Table 2. Summary of giant vacuoles (GVs) with I-pores across three flow-type areas.** GV counts were summed totals from eyes 1 and 2. GVs included were completely within the imaging field.

#### *GV types across flow-type areas*

Of 1312 GVs observed within the imaging field, the most frequently observed type of GV was the Type II GV, at 55.2% (N = 724) of overall GVs (Table 3). Type IV GVs were most frequently observed in high-flow areas, at 14.5% (N = 63) of all GVs; while non-flow areas had the smallest percentage of Type IV GVs, at 3.82% (N = 26). Type I GVs were most frequently observed in non-flow areas, at 48.2% (N = 328) of all GVs. A significant difference was found in the proportion of GV types I-IV among high-, low- and non-flow areas (Chi-square test  $\chi^2 = 118.12$ ,  $P \leq 0.01$ ).

Flow-Type Area	Eye	Type I	Type II	Type III	Type IV	Total
High	1	13 (15.7%)	63 (75.9%)	0 (0%)	7 (8.43%)	83
	2	92 (26.3%)	196 (56.0%)	6 (1.71%)	56 (16.0%)	350
	Total	<b>105</b> <b>(24.2%)</b>	<b>259</b> <b>(59.8%)</b>	<b>6</b> <b>(1.4%)</b>	<b>63</b> <b>(14.5%)</b>	<b>433</b>
Low	1	24 (24.2%)	66 (66.7%)	1 (1%)	8 (8.08%)	99
	2	15 (21.0%)	76 (78.4%)	0 (0%)	5 (5.15%)	97
	Total	<b>40</b> <b>(20.4%)</b>	<b>142</b> <b>(72.4%)</b>	<b>1</b> <b>(0.51%)</b>	<b>13</b> <b>(6.63%)</b>	<b>196</b>
Non	1	140 (44.0%)	172 (54.0%)	1 (0.31%)	5 (1.57%)	318
	2	188 (51.7%)	151 (41.5%)	5 (1.37%)	19 (5.22%)	363
	Total	<b>328</b> <b>(48.2%)</b>	<b>323</b> <b>(47.4%)</b>	<b>6</b> <b>(0.88%)</b>	<b>26</b> <b>(3.82%)</b>	<b>681</b>
Overall		473 (36.0%)	724 (55.2%)	13 (0.99%)	102 (7.8%)	1312

**Table 3. Summary of giant vacuole types across three-flow type areas.**

### **Comparison of giant vacuole number and size at 7 and 15 mmHg**

#### *GVs with and without I-pores across flow-type areas at 7 versus 15 mmHg*

A total of 3302 GVs were observed completely within the imaging field at 15 mmHg (.166 mm<sup>2</sup> inner wall surface area) compared to 1312 GVs at 7 mmHg (.200 mm<sup>2</sup> inner wall surface area). At 15 mmHg, high-flow areas had the highest number of GVs (N = 1284), followed by non-flow areas (N = 1227) and low-flow areas (N = 791) (Table 3). In contrast, at 7 mmHg, non-flow areas had the highest number of GVs (N = 681), followed by high-flow areas (N = 433) and low-flow areas (N = 196). In each flow-type area, there were more GVs at 15 mmHg, with approximately 3 times as many GVs in high-flow areas, approximately 4 times as many GVs in low-flow areas, and approximately 1.8

times as many GVs in non-flow areas when compared with the GVs at 7 mmHg. When comparing high-flow areas, GVs with I-pores were more frequently observed at 15 mmHg (18.6%) than at 7 mmHg (15.9%) (Table 4). Conversely, when comparing non-flow areas GVs without I-pores were more frequently observed at 7 mmHg (95.6%) than at 15 mmHg (90.7%). Both 7 and 15 mmHg showed a trend of a decreasing percentage of GVs with I-pores with the transition from high- to low- to non-flow areas. There was a significant difference in the overall percentage of flow-type areas at 7 versus 15 mmHg (Chi-square test  $\chi^2 = 9.59$ ,  $P \leq 0.01$ ).

Flow-Type Area	GVs with I-pores		GVs without I-pores		Total	
	7 mmHg	15 mmHg	7 mmHg	15 mmHg	7 mmHg	15 mmHg
High	69 (15.9%)	239 (18.6%)	364 (84.0%)	1045 (81.4%)	433	1284
Low	14 (7.1%)	124 (15.7%)	182 (92.9%)	667 (84.3%)	196	791
Non	32 (4.7%)	114 (9.3%)	651 (95.6%)	1113 (90.7%)	681	1227

**Table 4. Comparison of giant vacuoles with or without I-pores in three flow-type areas at 7 and 15 mmHg.** At each pressure, GV counts were summed totals from eyes 1 and 2. GVs included were completely within the imaging field.

#### *GV Types across flow-type areas at 7 versus 15 mmHg*

At both 7 and 15 mmHg, the overall most common GV type was the Type II GV, with 55.2% of GVs at 7 mmHg (N = 724) and 57.7% of GVs at 15 mmHg (N = 1904). Type IV GV were overall more common at 15 mmHg, with 11.9% of GVs (N = 392), versus 7.8% of GVs (N = 102) at 7 mmHg. Additionally, Type I GVs were overall more common at 7 mmHg, with 36.0% of GVs (N = 473), versus 27.9% of GVs at 15 mmHg (N = 921). There was an exceedingly low amount of Type III GVs at both 7 mmHg

(0.99%, N = 13) and 15 mmHg (2.6%, N = 85). A significant difference was found in the overall distribution of GV types at 7 and 15 mmHg (Chi-square test  $\chi^2 = 115.13$ ,  $P \leq 0.01$ ). When comparing individual GV types at 7 versus 15 mmHg, there was significant difference in the percentage of Type IV GVs (Chi-square test  $\chi^2 = 7.57$ ,  $P \leq 0.03$ ), Type II GVs (Chi-square test  $\chi^2 = 13.83$ ,  $P \leq 0.01$ ), and Type I GVs (Chi-square test  $\chi^2 = 84.22$ ,  $P \leq 0.01$ ). However, there was no significant difference in Type III GVs (Chi-square test  $\chi^2 = 3.066$ ,  $P = 0.22$ ).

Type IV GVs were more common in all flow-type areas at 15 mmHg. In high-flow areas, there were approximately 1.1 times as many Type IV GVs, and in low- and non-flow areas there were approximately 1.9 times as many Type IV GVs when compared with those at 7mmHg (Table 5).

The distribution of GV types was similar in high-flow areas at 7 and 15 mmHg (Fig. 14 & Table 5). When comparing GV type distributions in individual flow-type areas between 7 and 15 mmHg, there wasn't a significant difference in the percentage of GV types in high-flow regions (Chi-square test  $\chi^2 = 3.4724$ ,  $P = .324$ ), however there was a significant difference in the percentage of GV types in low- and non-flow regions (Low-flow Chi-square test  $\chi^2 = 17.01$ ,  $P \leq 0.01$ , Non-flow Chi-square test  $\chi^2 = 115.13$ ,  $P \leq 0.01$ ). In low-flow regions, there was a greater percentage of Type I GVs at 15 mmHg, Type II GVs at 7 mmHg, Type III GVs at 15 mmHg, and Type IV GVs at 15 mmHg. In

non-flow regions, there was a greater percentage of Type I GVs at 7 mmHg, Type II GVs at 15 mmHg, Type III GVs at 15 mmHg, and Type IV GVs at 15 mmHg.

Flow - Type Area	Eye	Type I (%)		Type II (%)		Type III (%)		Type IV (%)		Total	
		7 mm Hg	15 mm Hg	7 mm Hg	15 mm Hg	7 mm Hg	15 mm Hg	7 mm Hg	15 mm Hg	7 mm Hg	15 mm Hg
High - Flow	1	13 (15.7%) )	250 (25.6%) )	63 (75.9%) )	574 (58.9%) )	0 (0%) )	32 (3.3%) )	7 (8.43%) )	119 (12.2%) )	83	975
	2	92 (26.3%) )	50 (16.2%) )	196 (56.0%) )	171 (55.3%) )	6 (1.71%) )	5 (1.6%) )	56 (16.0%) )	83 (26.9%) )	350	309
	Total	<b>105</b> <b>(24.2%)</b> )	<b>300</b> <b>(23.4%)</b> )	<b>259</b> <b>(59.8%)</b> )	<b>745</b> <b>(58.0%)</b> )	<b>6</b> <b>(1.4%)</b> )	<b>37</b> <b>(2.9%)</b> )	<b>63</b> <b>(14.5%)</b> )	<b>202</b> <b>(15.7%)</b> )	<b>433</b>	<b>1284</b>
Low-Flow	1	24 (24.2%) )	167 (28.8%) )	66 (66.7%) )	329 (56.8%) )	1 (1%) )	21 (3.6%) )	8 (8.08%) )	62 (10.7%) )	99	579
	2	16 (21.0%) )	44 (20.8%) )	76 (78.4%) )	127 (59.9%) )	0 (0%) )	3 (1.4%) )	5 (5.15%) )	38 (17.9%) )	97	212
	Total	<b>40</b> <b>(20.4%)</b> )	<b>211</b> <b>(26.7%)</b> )	<b>142</b> <b>(72.4%)</b> )	<b>456</b> <b>(57.6%)</b> )	<b>1</b> <b>(0.51%)</b> )	<b>24</b> <b>(3.0%)</b> )	<b>13</b> <b>(6.63%)</b> )	<b>100</b> <b>(12.6%)</b> )	<b>196</b>	<b>791</b>
Non-Flow	1	140 (44.0%) )	105 (26.5%) )	172 (54.0%) )	248 (62.6%) )	1 (0.31%) )	11 (2.8%) )	5 (1.57%) )	32 (8.1%) )	318	396
	2	188 (51.7%) )	305 (36.7%) )	151 (41.5%) )	455 (54.8%) )	5 (1.37%) )	13 (1.6%) )	19 (5.22%) )	58 (7.0%) )	363	831
	Total	<b>328</b> <b>(48.2%)</b> )	<b>410</b> <b>(33.4%)</b> )	<b>323</b> <b>(47.4%)</b> )	<b>703</b> <b>(57.3%)</b> )	<b>6</b> <b>(0.88%)</b> )	<b>24</b> <b>(2.0%)</b> )	<b>26</b> <b>(3.82%)</b> )	<b>90</b> <b>(7.3%)</b> )	<b>681</b>	<b>1227</b>
Overall		<b>473</b> <b>(36.0%)</b> )	<b>921</b> <b>(27.9%)</b> )	<b>724</b> <b>(55.2%)</b> )	<b>1904</b> <b>(57.7%)</b> )	<b>13</b> <b>(0.99%)</b> )	<b>85</b> <b>(2.6%)</b> )	<b>102</b> <b>(7.8%)</b> )	<b>392</b> <b>(11.9%)</b> )	<b>1312</b>	<b>3302</b>

**Table 5. Giant vacuole (GV) population by pressure, flow-type area, and GV type.**

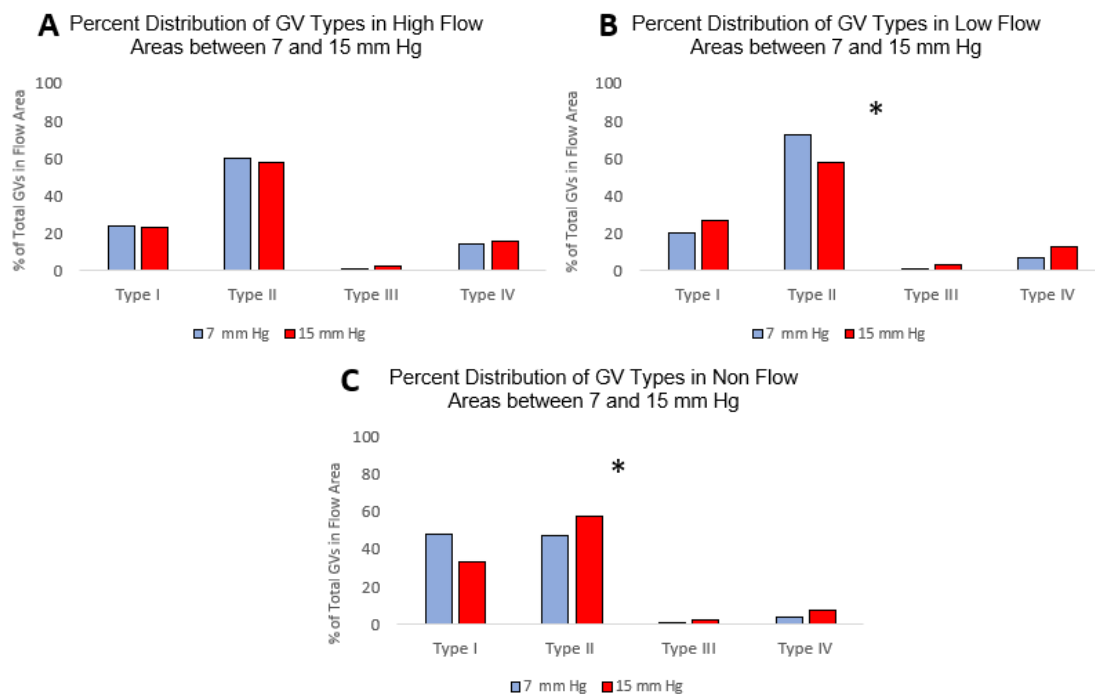


**Figure 14. Percent distribution of giant vacuole (GV) types across flow-type regions at 7 and 15 mmHg.** A: Percent distribution of GV types in high-flow regions. B: Percent distribution of GV types in low-flow regions. C: Percent distribution of GV types in non-flow regions. Asterisk (\*) indicates statistically significant difference between 7 and 15 mmHg.

#### *Span of GVs with and without I-pores at 7 versus 15 mmHg*

At both 7 and 15 mmHg, the median span of GVs with I-pores (7 mmHg: 71.5 sections, IQR 50 – 98.25, 15 mmHg: 61 sections, IQR 42-86) was significantly larger than that of GVs without I-pores (7 mmHg: 33, IQR: 19-56, 15 mmHg: 27 sections, IQR 18-47) (7 and 15 mmHg: Wilcoxon rank-sum test,  $P \leq 0.01$ ) (Fig. 15). When comparing across perfusion pressures, GVs with and without I-pores were significantly greater in span at 7 mmHg versus GVs at 15 mmHg.

GVs with I-pores were significantly greater in span than GVs without I-pores in high- and non-flow areas at both 7 and 15 mmHg (Median span of GVs with pores in high-flow

7 mmHg: 67; without pores: 45. Median span of GVs with pores in high-flow 15 mmHg: 60; without pores: 26) (Median span of GVs with pores in non-flow 7 mm Hg: 72.5; without pores: 25. Median span of GVs with pores in non-flow 15 mm Hg: 61.5; without pores: 25). ( $P \leq 0.01$ ). Low-flow areas were omitted from span comparisons because of an insufficient sample size of GVs with pores at 7 mmHg ( $N = 14$ ). In high-flow areas, the median span of GVs with and without I-pores at 7 mmHg was slightly significantly greater than that of GVs with and without I-pores at 15 mmHg ( $P \leq 0.04$ ). In non-flow areas, median span of GVs with I-pores (7 mmHg: 72.5 sections, IQR 44.5 – 98.75. 15 mmHg: 61.5, IQR: 40.25 – 96) was significantly greater than GVs without I-pores (7 mmHg: 25 sections, IQR: 16 – 47. 15 mmHg: 25, IQR: 17 – 44) at 7 and 15 mmHg ( $P \leq 0.01$ ). In non-flow areas, there was no difference in the median span of GVs with I-pores ( $P = .399$ ) or without I-pores ( $P = .570$ ) at 7 versus 15 mmHg.

At both 7 and 15 mmHg, the median span of GV Types I, II and IV varied significantly (Kruskal-Wallis Tests,  $P \leq 0.01$ ). However, median span of Type IV GVs was significantly larger than that of Type II GVs, and median span of Type II GVs was significant larger than that of Type I GVs. When compared between two pressures, Type I GVs were greater in span at 15 mmHg (7 mmHg: 20 sections, IQR 24.5 – 67. 15 mmHg: 22 sections, IQR 15 – 32). Type II GVs were greater in span at 7 mmHg (7 mmHg: 41 sections, IQR 24.5 – 67. 15 mmHg: 31 sections (IQR: 19 – 54). Type IV GVs were greater in span at 7 mmHg (7 mmHg: 73 sections, IQR 57 – 101.75. 15 mmHg: 65

sections, IQR 46 – 93) (Pairwise Wilcoxon rank sum test,  $P \leq 0.01$ ). Type III GV's were omitted from span comparisons because of insufficient sample size at 7 mmHg ( $N = 13$ ).

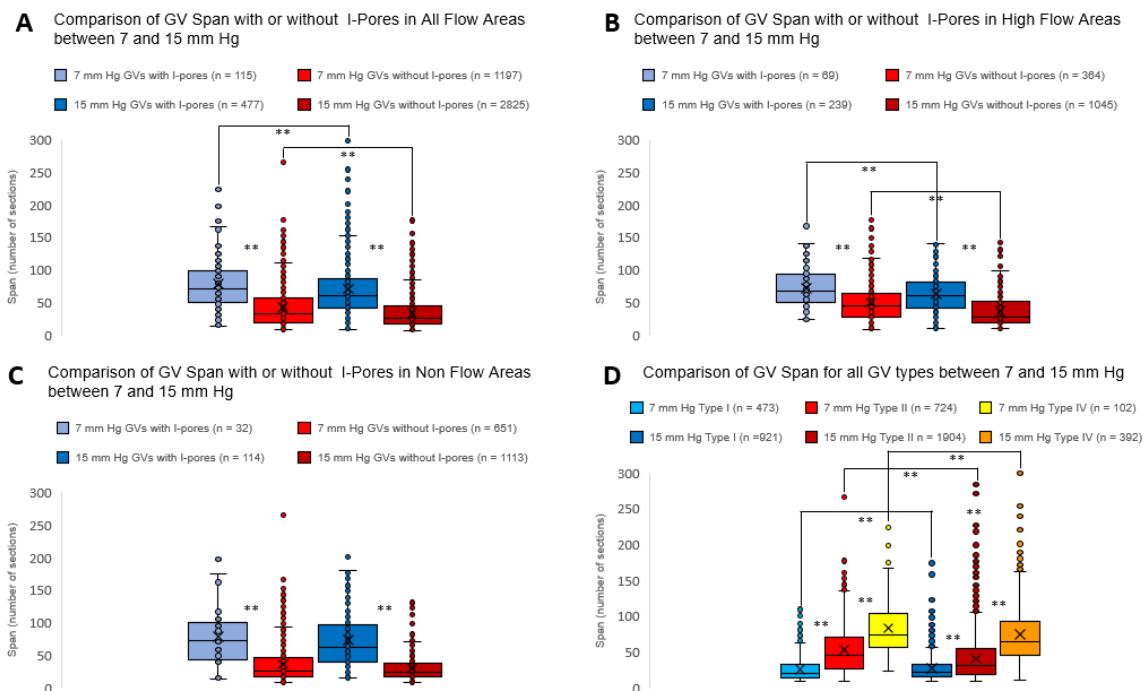


**Figure 15. GV spans across flow type regions and pressures.**

A: Span of giant vacuoles with and without pores across all flow-type areas at 7 versus 15 mm Hg. Median span of GV's with I-pores at 7 and 15 mmHg was greater than median span of GV's without I-pores. GV's with and without I-pores at 7 mm Hg had a significantly greater span than GV's with and without I-Pores at 15 mm Hg ( $P \leq 0.01$ ). B: Span of giant vacuoles with and without pores at high-flow areas at 7 versus 15 mmHg. Median span of GV's with I-pores at 7 and 15 mmHg was significantly larger than GV's without I-pores at 7 and 15 mmHg. When comparing across flow types between perfusion pressures of 7- and 15-mm Hg, median span of GV's with I-pores was significantly greater at 7 mm Hg than 15 mm Hg ( $P \leq 0.04$ ). Also, median span of GV's without I-pores was significantly greater at 7 mm Hg than 15 mm Hg ( $P \leq 0.01$ ). C: Span of giant vacuoles with and without pores at non-flow type areas at 7 versus 15 mm Hg. Median span of GV's with I-pores was significantly larger than GV's without I-pores at both 7 and 15 mmHg. There was no significant difference in the span of GV's with I-pores at 7 versus 15 mm Hg ( $P = .399$ ), or without I-pores ( $P = .570$ ). D: At 7 and 15 mmHg, Type IV GV's were greater in span than Type II GV's which were greater in span than Type I GV's. Type I GV's were greater in span at 15 mmHg, Type II GV's were greater in span at 7 mmHg, and Type IV GV's were greater in span at 7 mmHg.

#### *Volume of GV's at 7 versus 15 mmHg*

Overall, at both 7 and 15 mmHg, the median volume of GV's with I-pores (7 mmHg:

100.4  $\mu\text{m}^3$ , IQR 39.1 – 207.4, 15 mmHg: 117.3  $\mu\text{m}^3$  IQR 55.7 – 225.1) was greater than

that of GV's without I-pores (7 mmHg 12.56  $\mu\text{m}^3$ , IQR 3.9 – 43.9. 15 mmHg: 54.8  $\mu\text{m}^3$ ,

IQR 11.5 – 173.6) (Wilcoxon-rank sum test,  $P \leq 0.01$ ) (Fig. 16). When comparing across perfusion pressures, there was no significant difference in the volume of GVs with I-pores ( $P = .109$ ), however GVs without I-pores were significantly larger at 15 mmHg ( $P \leq 0.01$ ).

In high-flow areas, GVs with I-pores (7 mmHg:  $83.7 \mu\text{m}^3$ , IQR 36 – 148.6. 15 mmHg:  $172.4 \mu\text{m}^3$ , IQR 54.5 – 213.9) were significantly larger in volume than GVs without I-pores at both 7 and 15 mmHg.

In high-flow areas, there was no significant difference between GVs with ( $P = .07$ ) or without I-pores ( $P = .06$ ) when comparing between 7 and 15 mmHg. The trend in non-flow areas reflected the overall median volume trend, in that GVs with I-pores were similar in size, but GVs without I-pores were significantly greater in median volume at 15 mmHg ( $P \leq 0.01$ ). Low-flow areas were omitted from volume comparisons because of inadequate sample size.

Median GV volumes varied significantly among Type I, II, and IV GVs at both perfusion pressures (Kruskal-Wallis test,  $P \leq 0.01$ ). Type IV GVs were greater in volume than Type II GVs, which were greater in volume than Type I GVs. When comparing GV types across perfusion pressures, Type I and Type II GVs were significantly greater in volume at 15 mmHg than 7mmHg (Wilcoxon rank-sum test,  $P \leq 0.03$ ), but Type IV GVs were similar in volume across perfusion pressures, and there was no significant difference.

Type III GV's were omitted from volume comparisons because of insufficient sample size.

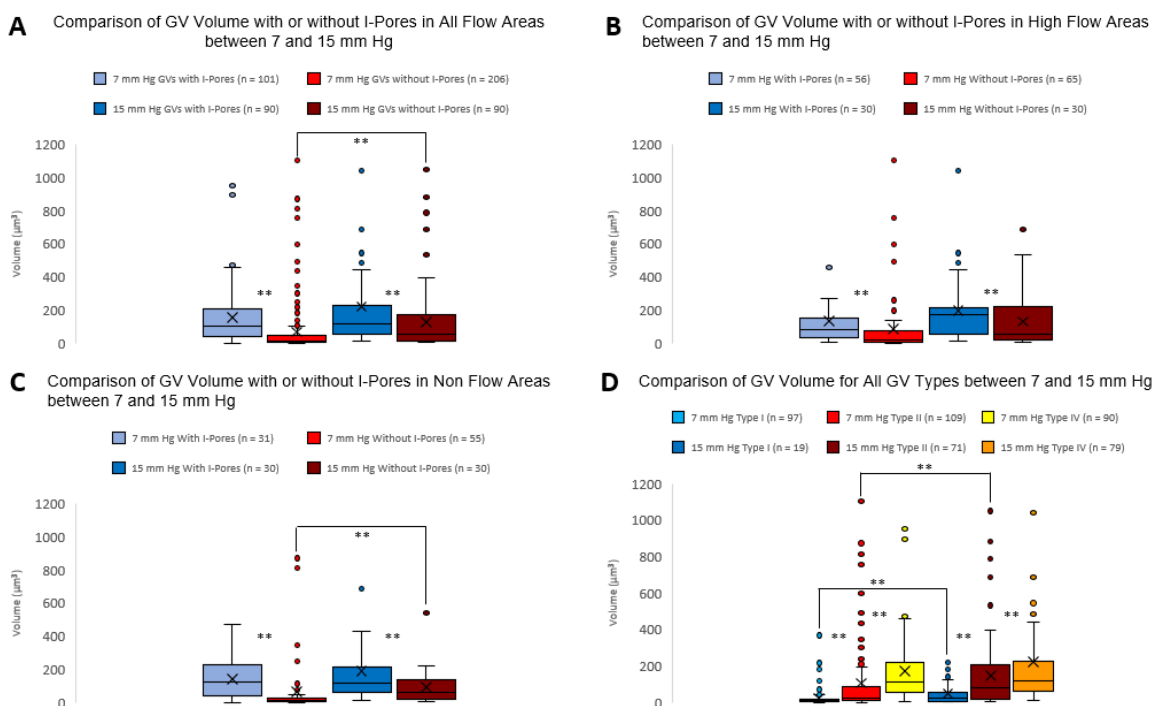


**Figure 16. Volume of giant vacuoles with and without pores across all flow types at 7 versus 15 mm Hg.**

A: Median volume of all GVs with I-pores was significantly greater than median volume of all GVs without I-pores at both 7 mm Hg and 15 mmHg. The median volume of GVs with I-pores wasn't significantly different at 7 versus 15 mmHg ( $P = .109$ ). The median volume of GVs without I-pores was significantly greater at 15 mm Hg ( $P \leq 0.01$ ). B: Volume of giant vacuoles with and without pores at high flow type areas at 7 versus 15 mm Hg. Median volume of GVs with I-pores at 7- and 15-mm Hg was significantly larger than GVs without I-pores at 7- and 15-mm Hg. When comparing GV volume at 7 versus 15 mm Hg, there was no significant difference between GVs with I-pores ( $P = .07$ ), and GVs without I-pores ( $P = .06$ ). C: Volume of giant vacuoles with and without pores at non-flow type areas at 7 versus 15 mm Hg. Median volume of GVs with I-pores was significantly larger than GVs without I-pores at both 7- and 15-mm Hg. When comparing GV volume at 7 versus 15 mm Hg, there was no significant difference in the median volume of GVs with I-Pores ( $P = .71$ ), however, GVs without I-pores were significantly larger at 15 than 7 mm Hg ( $P \leq 0.01$ ). D: At 7- and 15-mm Hg, there were significant differences between each GV Type ( $P < .01$ ). When comparing volume at 7- and 15-mm Hg, the median volume of Type I GVs was significantly greater at 15 mm Hg ( $P < .03$ ). The median volume of Type II GVs was significantly greater at 15 mm Hg ( $P < .01$ ). The median volume of Type IV GVs was not significantly different at 7- and 15-mm Hg.

### *Comparison of Type II GV Volume at 7 and 15 mmHg*

We further compared the volume distribution of the 3D reconstructed subset of GVs that were categorized as Type II GVs. While we observed a similar overall percentage of Type II GVs at 7 mmHg (55.2%,) and 15 mmHg (57.7%), we observed a significant difference in the volume distributions of Type II GVs (Two sample Kolmogorov-Smirnoff test,  $P \leq 0.01$ ).

The histogram bin containing median Type IV GV volumes (7 mmHg:  $113.6 \mu\text{m}^3$ , 15 mmHg:  $119.7 \mu\text{m}^3$ ) was used to approximate the volume of GV at which pores were most likely to be present. We observed a greater percentage of 3D reconstructed Type II GVs with a volume less than that of the median Type IV GV volume histogram bin. When comparing across perfusion pressures, we found a greater percentage of reconstructed Type II GVs with a volume less than that of the median Type IV GV volume histogram bin at 7 mmHg (78.0%) versus 15 mmHg (59.6%). Additionally, a noteworthy comparison is the difference in the percentage of 3D reconstructed Type II GVs in the volume range of 0-20  $\mu\text{m}^3$ . At 7 mmHg, 43.1% of 3D reconstructed Type II GVs were within this volume range, while at 15 mmHg, 25.7% of reconstructed Type II GVs were within this volume range (Figure 17).

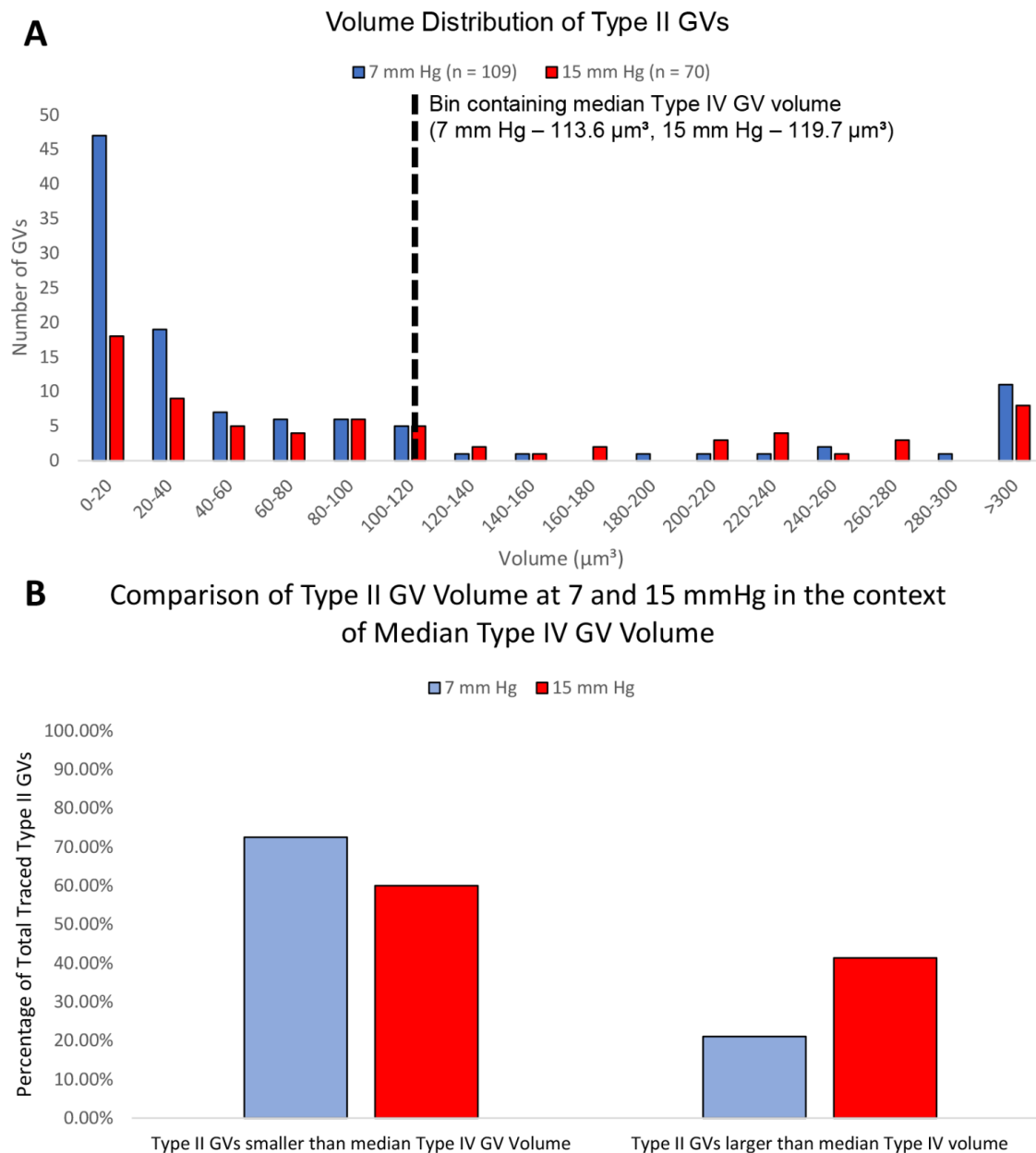


**Figure 17. Comparison of Type II GV Volume distribution between 7 and 15 mmHg** A: Type II GV volume distribution at 7 and 15 mmHg. Dashed line indicates the bin containing the median Type IV GV volume at both 7- and 15-mm Hg, which was used to approximate the threshold volume for pore formation. B: Distribution of early and late GV volume of Type II GVs at 7 and 15 mmHg. Type II GVs from 0 – 120  $\mu\text{m}^3$  were considered smaller than median Type IV GV volume, while GVs from 120 - >300  $\mu\text{m}^3$  were considered larger than median Type IV GV volume.

## Discussion

### *Overview and main findings*

In this study, we investigated the number and size of GVs in inner wall endothelium of SC at physiologic (7 mmHg) and compared the GV data at 7 mmHg with the GV data at elevated (15 mmHg) pressure from a previous study (Swain, 2021). At physiologic pressure, we analyzed 1312 GVs over 9586 images (0.166 mm<sup>2</sup> IW surface area). A similar number of images (9802 images, 0.200 mm<sup>2</sup> IW surface area) at elevated pressure (including 3302 GVs) were used to compare difference in the number and size of GVs between 7 and 15 mmHg. Our main findings were:

1. GVs are more populous at elevated pressure.
2. GVs with pores were greater in size than GVs without pores at both pressures.
3. GVs with I-pores did not differ in volume at physiologic versus elevated pressure, but GVs without I-pores were greater in volume at elevated pressure.
4. There were more Type IV GVs in the high-flow than low and non-flow areas at both pressures.

### *Increased number in GVs at elevated pressure*

Previous studies have investigated the relationship between IOP and IW endothelium morphology in monkey eyes (Grierson & Lee, 1977, 1978); and human eyes (Johnstone & Grant, 1973). Grierson & Lee observed an approximately linear relationship between GV number and IOP in the range of 8 to 30 mmHg in monkey eyes. Because our study used enucleated eyes for perfusion, the absence of episcleral venous pressure allows an

equivalent comparison to be made between our eyes perfused at 7 and 15 mmHg and Grierson & Lee's *in vivo* eyes perfused at 15 and 22 mmHg respectively (episcleral venous pressure is approximately 8-10 mmHg (Gaasterland & Pederson, 1983; Sit & McLaren, 2011)). At elevated pressure, Grierson & Lee counted roughly 1.5 times as many GVs in monkey eyes, while we observed roughly 2.5 times as many GVs in human eyes. Numerous factors could account for this difference, including the approximation technique used in Grierson and Lee's investigation, the limited resolution provided by light microscopy, and difference in species. In our study, SBF-SEM was used, which provided two advantages in this respect, increased resolving power and a more comprehensive 3D image that allowed us to classify small GVs. Further studies using SBF-SEM at higher pressures (30, 45 mmHg) of normal eyes and similar pressures (7, 15mmHg) of glaucomatous eyes are warranted to investigate the relationship between IOP and GV number and size in normal eyes as well as whether Type IV GVs decreases in glaucomatous eyes between the same pressures

#### *Relationship between GV size and I-pore formation*

Our findings were consistent with the hypothesis that increasing size of a GV play a role in I-pore formation through biomechanical strain (Braakman et al., 2014; D. L. Swain et al., 2021). We found GVs with I-pores to be greater in span and volume than GVs without I-pores in all flow type areas and at both pressures. Moreover, Type IV GVs were greater in span and volume than Type II and Type I GVs. At both pressures, we noticed differences in the percentage of GVs with I-pores across flow type areas. Consistent with models of segmental flow, there was a greater percentage of Type IV

GVs in high flow areas at both 7 and 15 mmHg compared to low and non-flow areas. The overall percentage of Type IV GVs was higher at 15 mmHg (11.9%) versus 7 mmHg (7.8%), suggesting increased aqueous outflow as pressure increases from 7 to 15mmHg. Additionally, the percentage of Type IV GVs was higher in each flow type area at elevated pressure. This could be related to the increased pressure gradient across the IW endothelium.

#### *Increased GV volume at elevated pressure*

Grierson & Lee observed an increase in GV volume as pressure increases in the range of 8 – 30 mmHg (Grierson & Lee, 1977). While trend refers to the overall increase in GV volume, we were interested to see if this trend also applied to individual GV types. We found that GVs with I-pores had similar volumes at physiologic and elevated pressures. GVs without I-pores, however, were significantly larger at an elevated pressure in non-flow areas as well as overall. Type IV GVs were also comparable in volume across pressures, while Type I and II GVs were larger in volume at elevated pressure. Our results may indicate a threshold size for pore formation. After a GV reaches this volume, the lining cellular member of GVs stretched thinner enough at certain location of a GV, a pore formation may be more likely to occur. After pore forms, the GV will cease to increase in volume. The greater median volume of GVs without I-pores at an elevated pressure indicates a higher presence of Type II GVs that appear temporally close to pore formation (close to the median volume of Type IV GVs).

*Increase in GV volume despite decrease in GV span at elevated pressure*

While we noticed an overall increase in volume in GVs without I-pores at elevated pressure that is consistent with Grierson and Lee's findings, we did not notice an increase in overall GV span at elevated pressure. In fact, GVs with and without I-pores were greater in span at physiologic pressure. This is not consistent with Grierson and Lee's study, in which they noticed increased GV dimensions including length, which is analogous to our span measurement, at elevated pressure (Grierson & Lee, 1977). Over 1312 GVs at 7 mm Hg in enucleated human eyes, the average GV length was 5.85  $\mu\text{m}$ , and over 3302 GVs at 15 mm Hg in enucleated human eyes the average GV length was 5.37  $\mu\text{m}$  (GV length formula = span x section thickness (0.13  $\mu\text{m}$ )). Over 2253 GVs in 9 animals at 15 mm Hg in live rhesus monkey eyes (comparable to 7 mm Hg in enucleated human eyes without episcleral venous pressure), the average GV length was 5.23  $\mu\text{m}$ . Over 1378 GVs in 3 animals at 22 mm Hg in live rhesus monkey eyes, the average GV length was 6.36  $\mu\text{m}$ . Grierson and Lee may have noticed an increase in length because they did not have enough resolving power to image to analyze small GVs, or because they used thicker tissue sections than we used. Our findings suggest changes in IW endothelial cell structure at an elevated pressure. Lai et al. found a significant decrease in IW/JCT cell-cell connections at eyes perfusion-fixed at 15 mm Hg versus eyes immersion-fixed at 0 mm Hg (Fig. 18) (Lai et al., 2019). This decrease in cell-cell connections could be related to the increase in GV volume despite a decrease in GV length as pressure was elevated, manifesting as a change in GV shape as IW endothelial cells go from flat to "ballooning" out into SC. A future study that analyzes changes in

both GV morphology and IW/JCT cell connections with increased perfusion pressure is warranted.

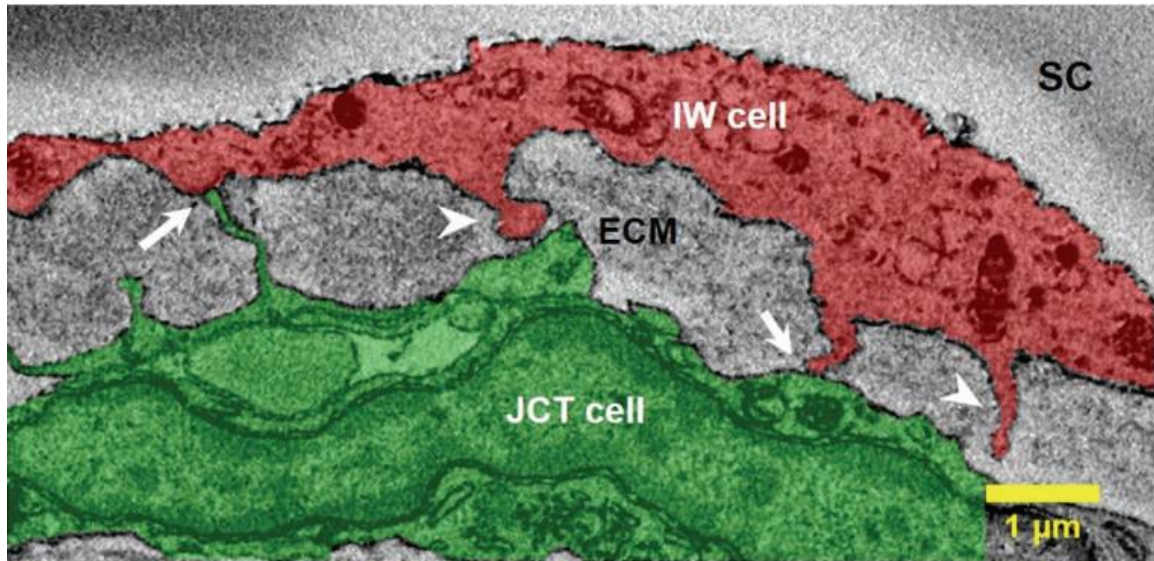


**Figure 18. Inner wall (IW) and juxtacanalicular (JCT) cell to cell connections.** One section from a block of tissue prepared for serial block-face scanning electron microscopy is shown. Connections between processes of an IW cell and a JCT cell are shown (white arrows). Additionally, processes of the IW cell that are not forming connections with the JCT cell are shown (white arrowheads) (From Lai et al, 2019).

#### *Study Limitations*

A major limitation of our study is the inability to follow the progression of a giant vacuole from formation to termination. Working with fixed tissue provides a fragmentary view of vacuolation and assumptions are made regarding the life cycle of GVs. For example, when examining a large Type II GV we are unable to decide whether pore formation is about to occur, the pore has already closed. Using an in-vitro model, Pedrigi et al. noticed giant-vacuole-like structures (GVLs) “migrating” about the cell layer, and larger GVLs forming from the agglomeration of smaller clustered GVLs (Pedrigi et al., 2011). This is another phenomenon that is difficult to visualize using a “static” imaging technique such as SBF-SEM. A technique that allows for real-time, high resolution, in

vivo visualization presents an ambitious goal that may provide novel insights into the dynamic processes of vacuolation and pore formation.

Another limitation of our study is the small sample size ( $n = 2$ ) of human eyes at each pressure. We noticed significant variability in GV number across donors, the most extreme example found when comparing high-flow areas in eyes 1 (83 GVs) and 2 (350 GVs) at physiologic pressure, more than 4 times as many GVs were found in eye 2.

Variability in GV number and size across donors has been reported in previous studies (Pedrigi et al., 2011). While a larger sample size would be beneficial, the time required to label, categorize, and trace GVs is significant, and automation of this process would be desirable. While exploring deep learning as an automation technique, we struggled to develop a workflow to manage the size of the dataset (at least 3 TB).

While we noticed an increased number and percentage of GVs with I-pores at an elevated pressure, this information alone doesn't allow for quantification of outflow facility. The hydrodynamic interactions between the porous JCT region and the IW of SC greatly increase the resistance that AH encounters as it drains the eye, due to the funneling effect experienced by AH as it moves through regions of JCT proximal to IW cell pores (Johnson et al., 1992). It may be valuable to investigate the location of GVs with I-pores throughout a block of tissue relative to each other, and then generate a 3D topographical map of these locations. This information could be obtained using SBF-SEM and

compared across flow-type areas and perfusion pressures and provide further insight into mechanisms of resistance generation along the conventional outflow path.

### *Concluding Summary*

In summary, we investigated the difference in size and types of GVs between physiologic and elevated (glaucoma-inducing) pressure using SBF-SEM and 3D reconstruction. Comparing both pressures, the volume of GVs with I-pores were similar, while the volume of GVs without I-pores were larger at elevated pressures. This may indicate a threshold size of GVs for pore formation. GVs with I-pores were significantly larger than GVs without I-pores in all flow-type areas at both pressures suggesting that larger size of GVs is a contributing factor for GV-associated I-pore formation. More Type IV GVs observed in the high-flow areas at both pressures suggest that Type VI GV formation may play a role in regulating segmental outflow and increasing this type of GV may increase the total high-flow area to relieve elevated interocular pressure in glaucoma.

**BIBLIOGRAPHY**

- Allingham, R. R., de Kater, A. W., Ethier, C. R., Anderson, P. J., Hertzmark, E., & Epstein, D. L. (1992). The relationship between pore density and outflow facility in human eyes. *Investigative Ophthalmology & Visual Science*, *33*(5), 1661–1669.
- Allison, K., Patel, D., & Alabi, O. (2020). Epidemiology of Glaucoma: The Past, Present, and Predictions for the Future. *Cureus*, *12*(11), e11686–e11686. PubMed. <https://doi.org/10.7759/cureus.11686>
- Braakman, S. T., Pedrighi, R. M., Read, A. T., Smith, J. A. E., Stamer, W. D., Ethier, C. R., & Overby, D. R. (2014). Biomechanical strain as a trigger for pore formation in Schlemm's canal endothelial cells. *Experimental Eye Research*, *127*, 224–235. <https://doi.org/10.1016/j.exer.2014.08.003>
- Cha, E. D. K., Xu, J., Gong, L., & Gong, H. (2016). Variations in active outflow along the trabecular outflow pathway. *Experimental Eye Research*, *146*, 354–360. PubMed. <https://doi.org/10.1016/j.exer.2016.01.008>
- Chaum, E., & Freddo, T. F. (2017). Anatomy of the Eye and Orbit: The Clinical Essentials. *Optometry and Vision Science*.
- Chen, W., Hu, T., Xu, Q., Chen, Z., Zhang, H., & Wang, J. (2020). Acute Effects of Intraocular Pressure-Induced Changes in Schlemm's Canal Morphology on Outflow Facility in Healthy Human Eyes. *Investigative Ophthalmology & Visual Science*, *61*(8), 36–36. <https://doi.org/10.1167/iovs.61.8.36>

- Deerinck, T. J., Bushong, E., Thor, A., & Ellisman, M. (2010). NCMIR methods for 3D EM: A new protocol for preparation of biological specimens for serial block face scanning electron microscopy. *National Center for Microscopy & Imag Res*, 6–8.
- Ethier, C. R. (2002). The inner wall of Schlemm's canal. *Experimental Eye Research*, 74(2), 161–172. <https://doi.org/10.1006/exer.2002.1144>
- Ethier, C. R., Coloma, F. M., de Kater, A. W., & Allingham, R. R. (1995). Retroperfusion studies of the aqueous outflow system. Part 2: Studies in human eyes. *Investigative Ophthalmology & Visual Science*, 36(12), 2466–2475.
- Ethier, C. R., Kamm, R. D., Palaszewski, B. A., Johnson, M. C., & Richardson, T. M. (1986). Calculations of flow resistance in the juxtacanalicular meshwork. *Investigative Ophthalmology & Visual Science*, 27(12), 1741–1750.
- Gaasterland, D. E., & Pederson, J. E. (1983). Episcleral venous pressure: A comparison of invasive and noninvasive measurements. *Investigative Ophthalmology & Visual Science*, 24(10), 1417–1422.
- Gong, H., & Francis, A. (2014). Schlemm's Canal and Collector Channels as Therapeutic Targets. In *Innovations in Glaucoma Surgery* (pp. 3–25). Springer.
- Gong, H., Freddo, T. F., & Johnson, M. (1992). Age-related changes of sulfated proteoglycans in the normal human trabecular meshwork. *Experimental Eye Research*, 55(5), 691–709. [https://doi.org/10.1016/0014-4835\(92\)90174-q](https://doi.org/10.1016/0014-4835(92)90174-q)
- Gong, H., & Swain, D. L. (2020). Anatomy of the conventional aqueous outflow pathway. In *Current Developments in Glaucoma Surgery and MIGS* (pp. 1–38). Kugler.

- Grierson, I., & Lee, W. R. (1977). Light microscopic quantitation of the endothelial vacuoles in Schlemm's canal. *American Journal of Ophthalmology*, *84*(2), 234–246. [https://doi.org/10.1016/0002-9394\(77\)90857-1](https://doi.org/10.1016/0002-9394(77)90857-1)
- Grierson, I., & Lee, W. R. (1978). Pressure effects on flow channels in the lining endothelium of Schlemm's canal. A quantitative study by transmission electron microscopy. *Acta Ophthalmologica*, *56*(6), 935–952. <https://doi.org/10.1111/j.1755-3768.1978.tb03813.x>
- Johnson, M., Shapiro, A., Ethier, C. R., & Kamm, R. D. (1992). Modulation of outflow resistance by the pores of the inner wall endothelium. *Investigative Ophthalmology & Visual Science*, *33*(5), 1670–1675.
- Johnstone, M. A., & Grant, W. G. (1973). Pressure-dependent changes in structures of the aqueous outflow system of human and monkey eyes. *American Journal of Ophthalmology*, *75*(3), 365–383. [https://doi.org/10.1016/0002-9394\(73\)91145-8](https://doi.org/10.1016/0002-9394(73)91145-8)
- Kapetanakis, V. V., Chan, M. P. Y., Foster, P. J., Cook, D. G., Owen, C. G., & Rudnicka, A. R. (2016). Global variations and time trends in the prevalence of primary open angle glaucoma (POAG): A systematic review and meta-analysis. *British Journal of Ophthalmology*, *100*(1), 86. <https://doi.org/10.1136/bjophthalmol-2015-307223>
- Koudouna, E., Young, R. D., Overby, D. R., Ueno, M., Kinoshita, S., Knupp, C., & Quantock, A. J. (2019). Ultrastructural variability of the juxtacanalicular tissue along the inner wall of Schlemm's canal. *Molecular Vision*, *25*, 517.
- Lai, J., Su, Y., Swain, D. L., Huang, D., Getchevski, D., & Gong, H. (2019). The Role of Schlemm's Canal Endothelium Cellular Connectivity in Giant Vacuole

Formation: A 3D Electron Microscopy Study. *Investigative Ophthalmology & Visual Science*, 60(5), 1630–1643. <https://doi.org/10.1167/iovs.18-26011>

Le, T. D., Swain, D. L., Lai, J., Lam, C., & Gong, H. (2019). Changes in Pore Densities of the Inner Wall Endothelium of Schlemm's Canal with Increasing Pressures Using 3D Serial Block-Face Scanning Electron Microscopy. *Investigative Ophthalmology & Visual Science*, 60(9), 3182–3182.

Mäepea, O., & Bill, A. (1989). The pressures in the episcleral veins, Schlemm's canal and the trabecular meshwork in monkeys: Effects of changes in intraocular pressure. *Experimental Eye Research*, 49(4), 645–663.  
[https://doi.org/10.1016/s0014-4835\(89\)80060-0](https://doi.org/10.1016/s0014-4835(89)80060-0)

Pedrigi, R. M., Simon, D., Reed, A., Stamer, W. D., & Overby, D. R. (2011). A model of giant vacuole dynamics in human Schlemm's canal endothelial cells. *Experimental Eye Research*, 92(1), 57–66.  
<https://doi.org/10.1016/j.exer.2010.11.003>

Sit, A. J., & McLaren, J. W. (2011). Measurement of episcleral venous pressure. *Advances In Glaucoma Treatments: Dedicated to Carl Camras*, 93(3), 291–298.  
<https://doi.org/10.1016/j.exer.2011.05.003>

Swain, D. (2021). *The Role of Giant Vacuoles and Pores in the Endothelium of Schlemm's Canal in Regulating Segmental Aqueous Outflow*. Boston University.

Swain, D. L., Le, T. D., Yasmin, S., Fernandes, B., Lamaj, G., Dasgupta, I., Gao, Y., & Gong, H. (2021). Morphological factors associated with giant vacuoles with I-pores in Schlemm's canal endothelial cells of human eyes: A serial block-face

scanning electron microscopy study. *Experimental Eye Research*, 205, 108488.

<https://doi.org/10.1016/j.exer.2021.108488>

Swaminathan, S. S., Oh, D.-J., Kang, M. H., & Rhee, D. J. (2014). Aqueous outflow: Segmental and distal flow. *Journal of Cataract and Refractive Surgery*, 40(8), 1263–1272. PubMed. <https://doi.org/10.1016/j.jcrs.2014.06.020>

Tham, Y.-C., Li, X., Wong, T. Y., Quigley, H. A., Aung, T., & Cheng, C.-Y. (2014). Global prevalence of glaucoma and projections of glaucoma burden through 2040: A systematic review and meta-analysis. *Ophthalmology*, 121(11), 2081–2090. <https://doi.org/10.1016/j.ophtha.2014.05.013>

Tripathi, B. J., & Tripathi, R. C. (1974). Vacuolar transcellular channels as a drainage pathway for cerebrospinal fluid. *The Journal of Physiology*, 239(1), 195–206. <https://doi.org/10.1113/jphysiol.1974.sp010563>

**CURRICULUM VITAE**

